



Research paper



Tri-axial shaking table testing of lighting support systems with pulley friction dampers and integrated dummy masses

Tran-Van Han ^{a,d}, Sung Chan Kim ^b, Jiuk Shin ^c, Nguyen Huu Cuong ^{a,e}, Kihak Lee ^{a,*}

^a Deep Learning Architecture Research Center, Department of Architectural Engineering, Sejong University, 209 Neungdong-ro, Gwangjin-gu, Seoul 05006, Republic of Korea

^b Sehong Inc, Ltd, 16, Tapsil-ro 58, Giheung-gu, Yongin-si, Gyeonggi-do, 17084, Republic of Korea

^c Department of Architectural Engineering, Gyeongsang National University, Jinju-daero, Jinju-si, Gyeongsangnam-do 52828, Republic of Korea

^d Faculty of Civil Engineering, Mien Trung University of Civil Engineering, Tuy Hoa and Danang, Viet Nam

^e Department of Civil Engineering, Vinh University, Vinh 461010, Viet Nam

ARTICLE INFO

Keywords:

Seismic performance
Shaking table testing
Wireway vibration attenuation system
Dummy masses
Friction damper
Vibration attenuation

ABSTRACT

Investigating pulley wireway systems equipped with friction dampers as alternatives to traditional exposed raceway light fixtures, this study adheres to the ICC-ES AC156 standard and evaluates the impact of system mass and connector types on seismic behavior using shaking table tests. The key findings indicate that an increased system mass variably affects the fundamental frequency of the system, depending on the type of connectors. In terms of earthquake performance, direct connectors outperformed pole connectors in the original system configuration, and the addition of dummy masses significantly reduced seismic energy while stabilizing acceleration responses in pole connector systems. Moreover, the study underscores the critical importance of minimizing pole length in systems using pole connectors and adopting a lower mounting height in systems with direct connectors to improve seismic performance.

1. Introduction

Nonstructural components (NSCs) play a crucial role in buildings and industrial facilities, as they are systems and components attached to floors, roofs, and walls that are not part of the main load-bearing structural systems. Despite not being directly involved in the primary load-bearing function of the structure, NSCs are still susceptible to considerable seismic forces, thereby presenting a notable hazard during seismic events [1]. The Federal Emergency Management Agency (FEMA) E-74 has categorized NSCs into three major categories: (1) architectural components, (2) mechanical, electrical, and plumbing systems, and (3) furniture, fixtures, equipment, and other contents of the NSCs [2].

NSCs affect building floor acceleration demands, represented by peak floor accelerations (PFAs) and floor response acceleration spectra (FRS). Adam et al. [3] studied single-degree-of-freedom (SDOF) NSCs in relation to multi-degree-of-freedom (MDOF) structures. Villaverde et al. [4] introduced a method to estimate NSC responses considering both NSC and structural nonlinearity. Chaudhuri et al. [5] researched SDOF NSCs connected to code-compliant steel frames. Tamura et al. [6] found

that nonlinear SDOF NSCs reduce yield strength needs. Vukobratovic et al. [7] showed that NSC nonlinearity decreases FRS values. Obando et al. [8] analyzed nonlinear SDOF NSCs on MDOF structures regarding inelastic displacement ratios. Anajafi et al. [9] formulated spectra for acceleration-sensitive NSCs. Kazantazi et al. [10] suggested a method for lightweight nonlinear NSC strength reduction. The study by Vukobratovic et al. [11] delved into the seismic behavior of acceleration-sensitive non-structural components in a twelve-storey concrete building. The study examined the effects of structural vibration modes and the nonlinearity of non-structural components on floor acceleration demands in a twelve-storey concrete building. Additionally, a new method for determining peak floor acceleration was provided. Ruggieri et al. [12] observed the effect of diaphragm flexibility on accelerations in RC buildings with considering to NSCs as linear elastic.

On the other hand, NSCs are often susceptible to damage at seismic levels that might not affect the main structural components [13]. Research conducted by Kircher and Filiatrault emphasized the economic losses associated with NSC failures during earthquakes, including property loss, site clean-up, and replacement expenses, which often outweigh the losses resulting from structural damage [14,15]. For instance,

* Corresponding author.

E-mail address: kihaklee@sejong.ac.kr (K. Lee).

the 1989 Loma Prieta earthquake led to major damage in suspended ceilings and lighting systems at the San Francisco International Airport [16,17]. Similarly, the 1994 Northridge earthquake caused severe damage to emergency power systems in a key local hospital in Los Angeles [1]. Other examples include the 1985 Mexico Earthquake and the 2010 Haiti Earthquake, where electrical cabinets at critical facilities suffered significant damage [2]. Major public buildings in South Korea, such as hospitals, Korea train express (KTX) railway stations, and shopping malls, experienced degradation of electrical systems following the 2016 Gyeongju and 2017 Pohang earthquakes [18]. The 2012 Emilia earthquake revealed that cladding panel damage was widespread in precast structures [19]. Similar reports of massive damage caused by the collapse of NSCs were observed in earthquakes such as the 2010 Chile earthquake, 2011 Christchurch earthquake in New Zealand, 2011 Tohoku-Oki earthquake in Japan, 2013 Lushan earthquake in China, 2016 Kumamoto earthquake in Japan, and 2016 Central Italy earthquake [20–25]. Consequently, the study of the seismic behavior of NSCs is widely recognized as a critical component of earthquake risk mitigation.

In recent years, academic interest in enhancing the seismic performance of NSCs has grown. The study of NSCs has become increasingly important because of their role in buildings and industrial facilities and their vulnerability to seismic actions. Specifically, the seismic performance of nonstructural electrical components has been a significant focus. Researchers have aimed to understand the vulnerabilities of nonstructural electrical equipment during seismic events and improve their performance. Several important studies have provided insights into the seismic response and fragility of nonstructural electrical components. FEMA P-58 [26] provides a methodology for assessing the seismic performance of electrical components using fragility functions. Hwang et al. [27] conducted a seismic fragility analysis of electrical equipment in a typical electric substation in the eastern United States, utilizing actual earthquake damage data. Their study aimed to assess the vulnerability of electrical equipment to seismic forces and identify critical failure modes. Gupta et al. [28] proposed a novel method to accurately evaluate incabinet response spectra for the seismic qualification of electrical instruments. They found that typically only a few cabinet modes significantly affected spectral accelerations at crucial instrument locations. The significant mode often pertained to local cabinet components. The Rayleigh-Ritz method was used to calculate dynamic properties of these modes, offering significant time and effort savings compared to the finite element method. Rustogi et al. [29] discussed the Ritz vector approach for electrical cabinet dynamics, emphasizing its basis on one significant cabinet mode. The study noted discrepancies in the observed global rocking in anchored cabinets and proposed modifications for incorporating this observed rocking. Porter et al. [30] focused on evaluating the fragility of various types of electrical equipment commonly found in commercial and industrial buildings. Through their investigation, they aimed to quantify the probability of failure for different equipment categories under seismic loading conditions. A simplified model was developed by Cho et al. [31] to depict the nonlinear dynamic behavior of nuclear power industry cabinets during earthquakes. Using Duffing's restoring force, the model considered cabinet softening. Experiments on a real cabinet confirmed the softening behavior and showed material yielding wasn't a primary nonlinearity source. The model matched experimental data and offered computational efficiency without needing tests. Wang et al. [32] explored the seismic performance of a prototype diesel generator with a restrained vibration isolation system. They conducted quasi-static cyclic loading tests and shaking table tests to evaluate the response of the system. The results highlighted significant fatigue damage to the connection between the vertical restraint rods and the top plate, as well as pull-out failure of the vertical restraint rods as the primary failure mechanisms. Additionally, the study demonstrated that incorporating snubbers into the vibration isolation system could reduce the displacement response. Tran et al. [33] proposed a method to gauge electrical cabinet vulnerability in nu-

clear plants using fragility curves. They compared two fragility analyses for cabinets under different conditions and emphasized the importance of support boundary conditions in influencing cabinet acceleration response. Son et al. [34] performed shaking table tests to investigate the seismic qualification of an electrical cabinet. Their study highlighted that the seismic response of the cabinet system was more pronounced during high-frequency earthquakes compared to low-frequency ones. Understanding the frequency-dependent behavior of electrical cabinets is crucial for designing robust systems that can withstand a broad range of seismic events. In another study, Dinh et al. [35] conducted an experimental seismic investigation of a 1000 kVA cast resin-type hybrid mold transformer using a tri-axial shaking table test. Their findings revealed that the damage observed in the specimen was mainly attributed to the slipping of certain gaskets and the loosening of connecting bolts between the bed beam and the bottom beam. Understanding the failure mechanisms of transformers provides valuable insights into enhancing their seismic resilience. Jeon et al. [36] investigated the seismic behavior of electrical cabinets in Korea post the 2016 Gyeongju earthquake. They studied the rocking behavior and its impact on the dynamic properties of the cabinet, noting sensitivity to certain electrical instruments and frequency oscillations. Latif et al. [37] delved into the seismic assessment of equipment in Nuclear Power Plants, focusing on the role of anchor interaction in the seismic response of electrical cabinets. They underlined the significance of anchor bolt nonlinear interaction in the seismic response. Merino et al. [38] introduced a seismic classification system for acceleration-sensitive non-structural elements using shake table testing, exemplified on electrical cabinets in Italy. The classification accounted for varying seismic hazards and performance objectives.

Despite the integral role of lighting systems in building safety and illumination, advancements in their seismic performance remain limited. Han et al. [39] introduced a novel lighting support system reinforced with a pulley friction damper. This innovative system incorporated a wireway vibration attenuation system specifically designed for raceway light fixtures. Shaking table test revealed a significant reduction in seismic energy and peak oscillation, indicating the potential of this system as a seismic-resistant solution. In a subsequent investigation, Han et al. [40] evaluated the system's seismic performance concerning various connectors, employing the ICC-ES AC 156 standard.

While the prior research by Han et al. [39,40] has significantly advanced the understanding of the seismic performance of the innovative lighting support system reinforced with a pulley friction damper using direct connectors and pole connectors, there remain areas for exploration. The earlier study revealed that specimens with pole connectors displayed markedly greater earthquake energy compared to those with direct connectors, particularly in the lateral direction. As such, there is a need for further research to enhance the earthquake performance and stability of this innovative system, especially for those incorporating pole connectors.

In this study, the incorporation of dummy masses into the novel lighting system introduced by Han et al. was proposed with the objective of enhancing its seismic performance. Shaking table testing was conducted to analyze the dynamic response of the lighting support system under different configurations. The paper outlines the experimental methodology, presents the test results, and discusses the impact of additional mass on the seismic behavior of the lighting support system.

The remainder of this paper is organized as follows: Section 2 provides an overview of the experimental methodology adopted in this study. Section 3 discusses the test results highlighting the influence of mass on the seismic behavior of the lighting support system. Finally, Section 4 concludes the paper by summarizing the key findings and proposing future research directions to further advance the seismic performance of the novel lighting systems in buildings.

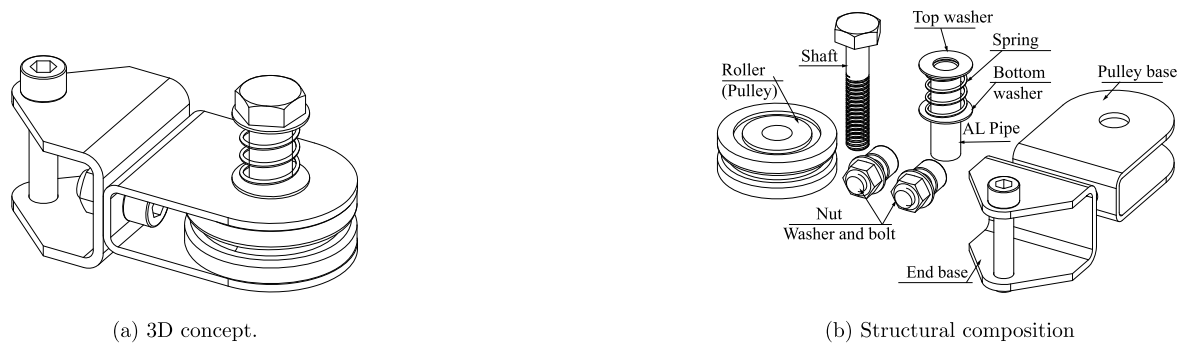


Fig. 1. Concept of a pulley friction damper.

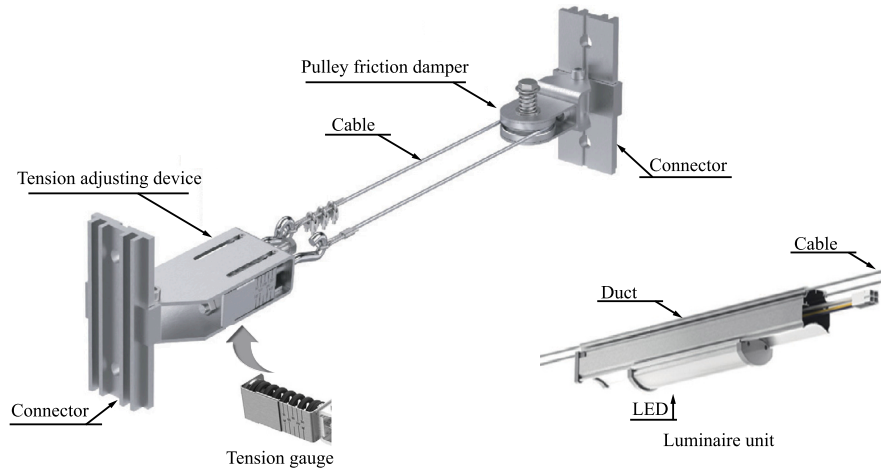


Fig. 2. Concept of the proposed vibration attenuation system.

2. Concept of the novel wireway vibration attenuation system

Fig. 1 illustrates the conceptual design of the pulley friction damper [39,40]. This damper is connected to the primary structure using a bolted attachment through an end base. The pulley base is affixed to the end base using two bolts, two nuts, and two washers, functioning as a foundation for the pulley itself. A combination of an aluminum pipe and a shaft allows the pulley to rotate around its vertical axis. Notably, the shaft's bottom end is threaded, facilitating its connection to the bottom hole of the pulley base. A cable, wound around the pulley, links the damper to the lighting system.

Fig. 2 shows the concept of the proposed vibration attenuation system.

The system's earthquake energy is mitigated through a frictional process facilitated by a pulley friction damper. This damper dissipates seismic energy by capitalizing on the mechanical friction between the pulley and its base, between the pulley and the aluminum pipe, and the friction between the cable and the pulley itself. The damper's seismic energy dissipation is regulated by a mechanism involving a spring that's coaxial with the pulley's rotation axis. This spring's two ends are set within a bottom washer and a top washer. The force the spring applies to the pulley determines the efficiency of the damper's seismic energy dissipation. This compression is modulated by altering the spring's length, which is done by adjusting the positions of the top washer and the shaft. Moreover, the damper's seismic energy dissipation efficiency can be fine-tuned by modifying the cable's tension using a towing machine situated at the system's opposite end.

In actual buildings, innovative lighting systems need to be anchored to the primary load-bearing elements of the structure, such as walls, beams, columns, and floors, using various connectors. Fig. 3 illustrates the conceptual design for connecting these systems to a Beam-column,

a Ceiling, a Wall, and an H-beam frame. These four types of connectors can be broadly categorized into two groups: the *pole connector* (used for Ceiling and Beam-column connections) and the *direct connector* (for Wall and H-Beam frame connections).

3. Shaking table test

3.1. Shaking table test frames

The seismic behavior of pulley wireway systems was investigated in this study using shaking table tests conducted at the Earthquake Disaster Prevention Research Center at Pusan National University. The table, measuring 4 × 4 meters, was designed to support up to 30,000 kg. Three key components were incorporated into the tests: (1) a simulator that was used to replicate earthquake motions; (2) a steel frame that was designed to transfer seismic excitations; and (3) specimens. Details are provided in Fig. 4.

For experiments, the steel frame was fabricated, simulating a room in the target building. The lower level had four steel beams and columns; the upper had a T-beam and two columns. For tri-axial shaking table tests across longitudinal (X), lateral (Y), and vertical (Z) axes, the test frame was designed to be sufficiently rigid, ensuring no inadvertent amplification of the table input motion [41,42]. The frame's rigidity was carefully ensured, maintaining its fundamental frequency even after integrating the mass of the lighting specimens. Resonance frequency search tests were conducted to determine the frame's natural frequency, detailed in Table 4. The findings indicate that the fundamental frequencies of the steel frame remained relatively consistent across the shaking table tests. Consequently, it was concluded that the frame possessed adequate rigidity to prevent inadvertent amplification of the table input motion within the testing frame.

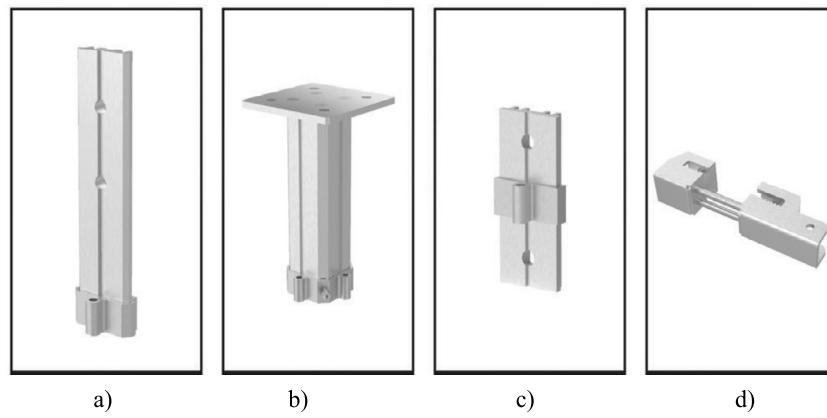
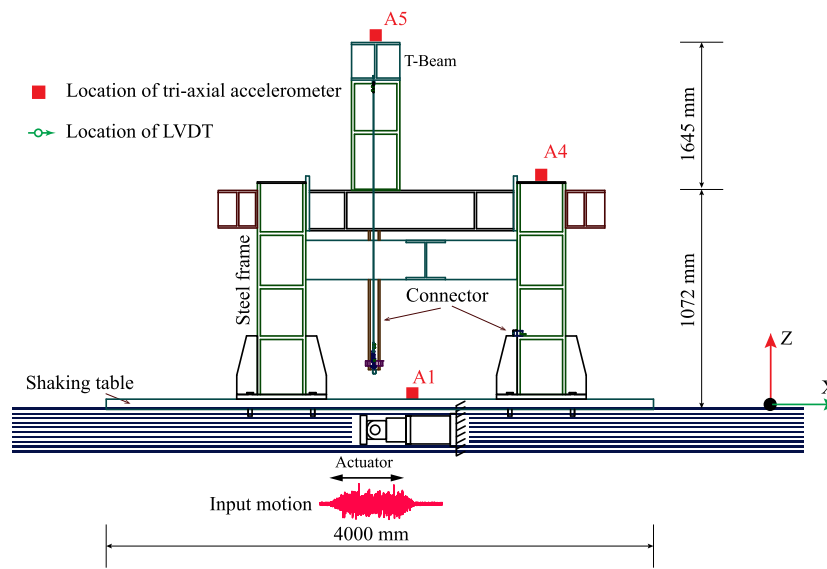
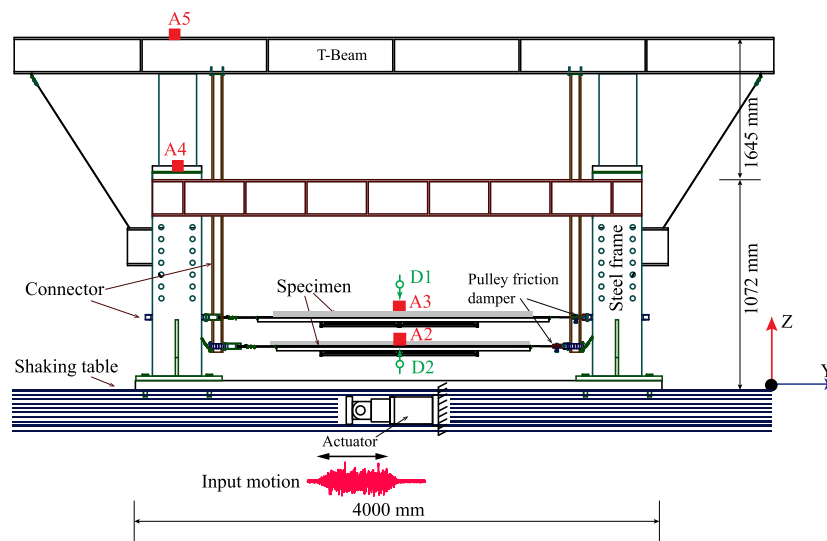


Fig. 3. The concept of the system's connections to the (a) Beam-column type (BCT); (b) Ceiling type (CT); (c) Wall type (WT); (d) H-beam frame type (HBT).



(a) Side view of test set-up.



(b) Front view of test set-up

Fig. 4. Shaking table test set-up.

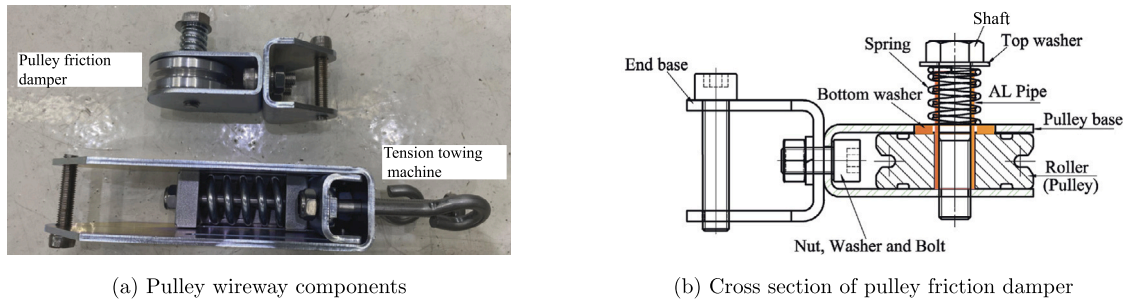


Fig. 5. The components of the pulley wireway system.

Table 1

Mechanical characteristics of the cable.

Item	value	units
Wire structure	7 × 7	-
Diameter	4	mm
Maximum load bearing	9.8	kN
Weight per unit length	0.066	kg/m
Displacement (50kgf tensile load)	0.7	mm
Modulus of elasticity	96105	MPa

3.2. Description of the test specimens

Four prototypes of a wireway system, each incorporating a dummy mass, were examined, each differentiated by its connector type: Ceiling (CT), H beam frame (HBT), Wall (WT), and Beam Column (BCT) [40]. The lighting system incorporated a 34 W LED light mounted on a 65 × 70 × 2500 mm aluminum duct, with a total length of 3680 mm. Prototypes were categorized as *pole connector* (CT and BCT) or *direct connector* (WT and HBT). The poles and duct were made from AL6063 alloy, while the pulley used AL6061 alloy. Stainless steel cables of 4 mm diameter were utilized, with their properties detailed in Table 1.

The information on the material properties of stainless steel and aluminum alloy is shown in Table 2 [40]. It is noted that the original mass of the lighting system primarily comprised the natural mass of essential components, including pipes, wiring, and electrical equipment, with a total mass of approximately 27 kg.

For each prototype, a friction damper featuring a 60 mm diameter pulley was incorporated. This friction damper serves the purpose of dissipating seismic energy through mechanical friction occurring between various interfaces, including the pulley and the pulley base, the cable and the pulley, as well as the pulley and the aluminum pipe [39]. The actual image of the pulley friction damper, along with the tension adjusting device, are depicted in Fig. 5.

Han et al. [40] conducted an investigation on four original distinct prototypes of a novel wireway system without dummy masses (see Fig. 6). In the current study, these four specimens, now augmented with a dummy mass of 40.5 kg, were further explored. Detailed information about these specimens is provided in Fig. 7.

The fundamental frequency of a single degree of freedom (SDOF) system can be calculated using the formula [43]:

$$f = \frac{1}{2\pi} \sqrt{\frac{k}{m}} \quad (1)$$

Where:

- f is the fundamental frequency of the system.
- k is the stiffness of the system.
- m is the mass of the system.

Based on Eq. (1), it is clear that adding dummy masses can adjust the fundamental frequencies of a novel lighting system. This study assessed the impact of such adjustments on the seismic response of the pulley

wireway system. Specimens were categorized as *WOD* (without dummy masses) and *WD* (with dummy masses) for analysis. The focus was on examining the frequency ratio r_f , defined as the ratio of the specimen's fundamental frequency f_s to the frame's fundamental frequency f_f .

$$r_f = \frac{f_s}{f_f} \quad (2)$$

3.3. Test setup and measuring instruments

To record acceleration and displacement responses in three orthogonal directions during tests, a comprehensive instrumentation setup was implemented. This setup included five tri-axial accelerometers (A1-A5) and two linear variable displacement transducers (LVDTs) (D1 and D2), each positioned at specific locations. Accelerometer A1, situated at the shaking table's base, measured base excitation. A5 and A4, positioned atop the T-beam and the first-floor steel column respectively, tracked the structural response. A2, A3, and LVDTs D1 and D2 were located at the duct's top midpoint, crucial for assessing specimen earthquake performance.

During testing, the CT and HBT specimens were evaluated in Steps 1 and 2, and the WT and BCT in Step 3, with the T-beam removed in the latter. The recorded acceleration and displacement data from these sensors were pivotal for a comparative analysis of the specimens' seismic behavior. The locations of the accelerometers and LVDTs are depicted in Fig. 8.

3.4. Input ground acceleration records

Shaking table tests followed the loading protocol recommended by ICC-ES-AC 156 [41], a standard for assessing the seismic performance of NSCs. The seismic input was designed to meet the required response spectrum (RRS)—a representation of the minimal seismic acceleration needed to stimulate a component based on its natural period or frequency. This RRS was informed by two key parameters: the story height ratio (z/h) and the design spectral response acceleration for short durations (S_{DS}) [44–46]. Calculations for the RRS levels incorporated seismic parameters, both horizontal and vertical spectral accelerations, for both flexible and rigid components, as illustrated in Fig. 9.

Where the horizontal spectral acceleration for flexible A_{FLX-H} and rigid A_{RIG-H} components are computed as follows [41,47]:

$$A_{FLX-H} = S_{DS} \left(1 + 2\frac{z}{h}\right) \leq 1.6S_{DS} \quad (3)$$

$$A_{RIG-H} = 0.4S_{DS} \left(1 + 2\frac{z}{h}\right) \quad (4)$$

The vertical spectral acceleration of the flexible A_{FLX-V} and rigid A_{RIG-V} components are computed as follows [41,47]:

$$A_{FLX-V} = 0.67S_{DS} \quad (5)$$

$$A_{RIG-V} = 0.27S_{DS} \quad (6)$$

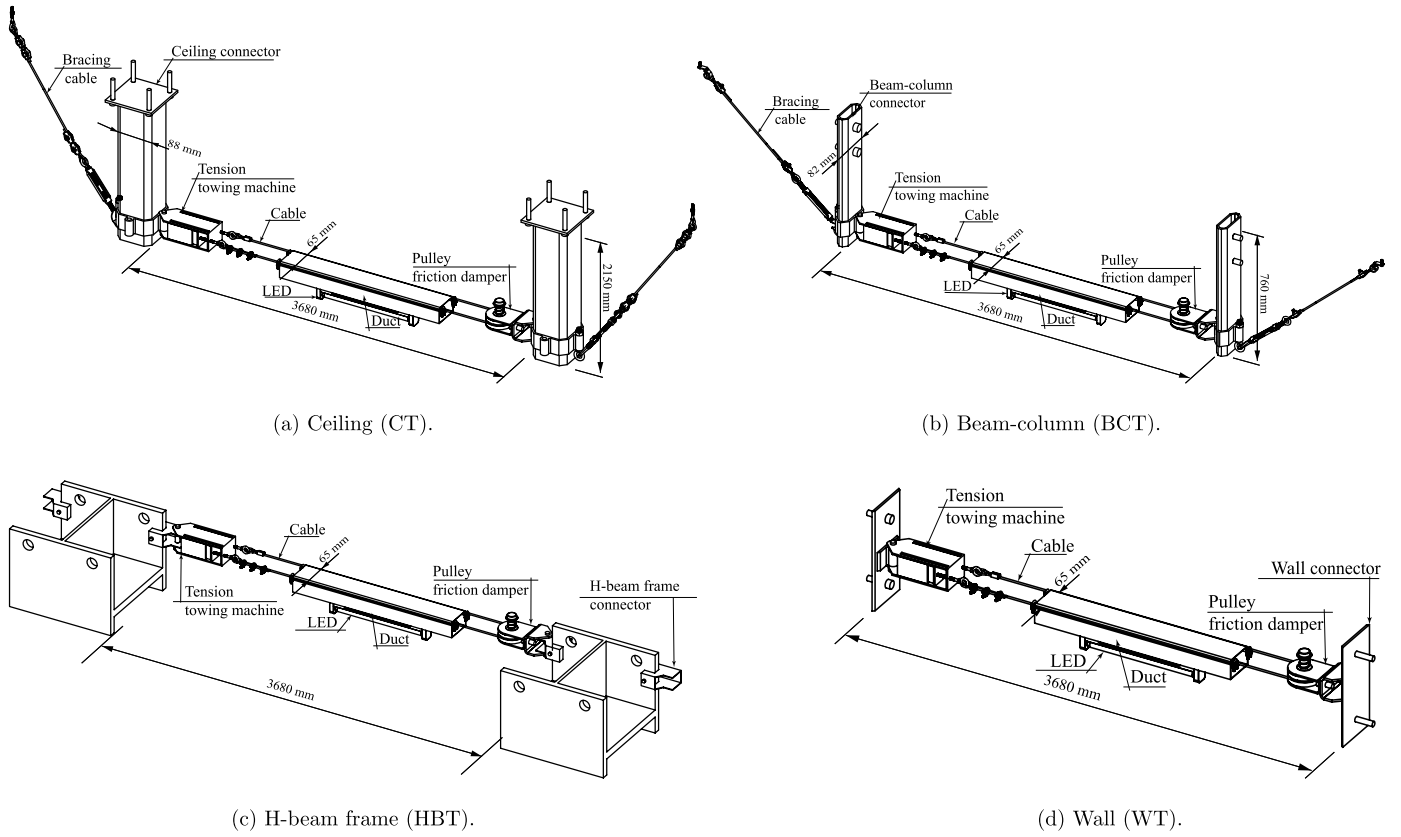


Fig. 6. Details of the four test specimens without dummy masses as described by Han et al. [40].

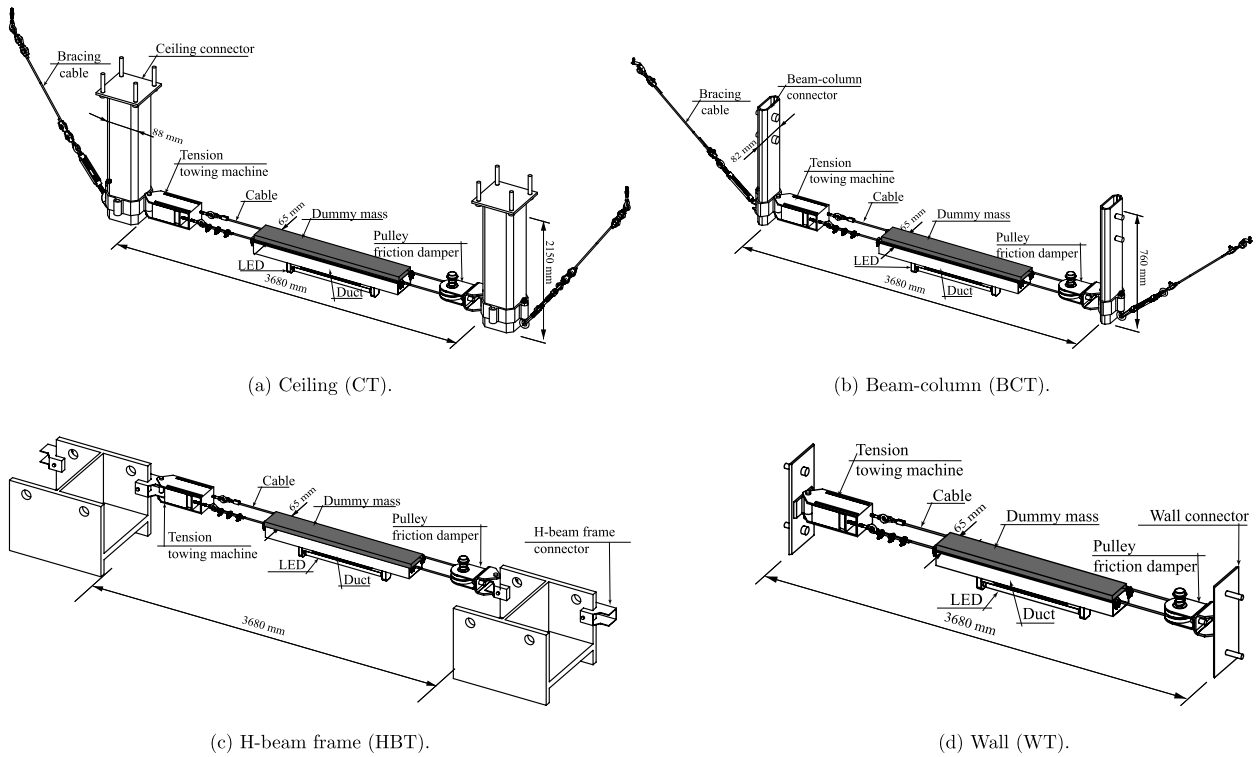


Fig. 7. Details of the four test specimens with dummy masses.

Table 2
Mechanical properties of all the main parts of the system.

Material	Density (g/cm ³)	Ultimate Strength (MPa)	Yield Strength (MPa)	Elongation at Break (%)	Elastic Modulus (GPa)	Poisson's Ratio
AL6063	2.70	150	90	20	69	0.33
AL6061	2.70	310	276	12-17	68.9	0.33

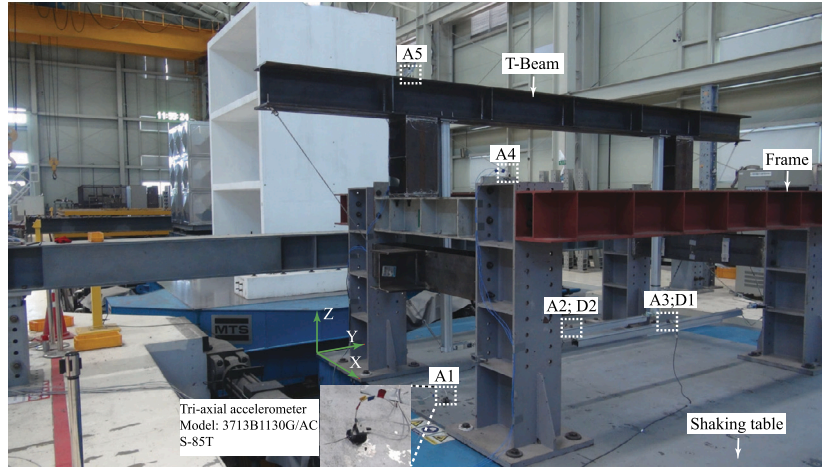


Fig. 8. The locations of the accelerometers and LVDTs from Steps 1 and 2.

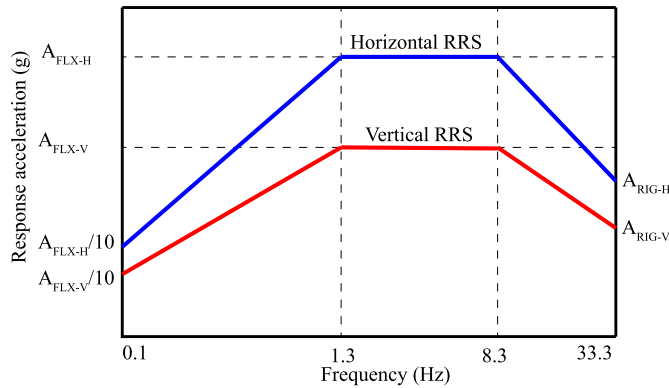


Fig. 9. Required response spectrum (AC156).

According to the Korean Design Standard [45] (KCSC 2019) and guidelines for calculating S_{DS} based on the peak ground acceleration with a 2400-year return period (S) of 0.19 in South Korea [47], Dinh et al. [35], Jun et al. [42], and Kim et al. [48] used a value of $S_{DS} = 0.50$ g, assuming a Site Class D (stiff) soil condition. For this study, an AC156 input motion equivalent to $S_{DS} = 0.5$ g was scaled using values derived from the standard, with scaling factors of 100% ($S_{DS} = 0.5$ g) and 140% ($S_{DS} = 0.7$ g). The test plan is detailed in Table 3.

In this research, the assumption made was that the specimens were affixed to the highest floor of structures, leading to a z/h ratio of 1.0. The input acceleration time-history, as well as its elastic response spectrum for 5% damping (referred to as the test response spectrum or TRS), the RRS, and the RRS scaled to 90% and 130%, are shown in Fig. 10. This input acceleration time-history was formulated by the engineers at the Seismic Research And Test Center of Pusan National University. The graph indicates that the input acceleration meets the standards set in ICC-ES AC156 and SPS-F KOCED 0007-7419:2021 [41,47].

4. Test results and discussion

4.1. Fundamental frequency of the specimens

4.1.1. Experimental results

Prior to the shaking table tests, resonance frequency search tests were conducted [40,39]. Single-axis sinusoidal sweeps were performed within the frequency range of 1.0 Hz to 50 Hz along each orthogonal major axis. The fundamental frequencies of the specimens were determined using the frequency domain transfer function technique [49]. Fig. 11 illustrates the transfer function charts for Steps 1, 2 and 3.

The fundamental frequency results for the four different specimens with dummy masses and the steel frame are shown in Table 4. The specimens with dummy masses displayed consistent fundamental frequency results. For the HBT specimen, frequencies were 2.25 Hz (X), 26 Hz (Y), and 4.00 Hz (Z). The CT specimen recorded frequencies of 4.75 Hz (X), 12.50 Hz (Y), and 4.25 Hz (Z). This consistency confirms the structural integrity of both specimens during the experiments, even with the added dummy masses.

The fundamental frequency results for the four different specimens with dummy masses are shown in Table 5 [40].

The experimental results indicate that the mass and stiffness of the dummy masses significantly influenced the fundamental frequencies of the novel system. The experimental findings revealed that in the X and Z directions, the specimens with dummy masses exhibited smaller fundamental frequency values compared to specimens without dummy masses, despite utilizing the same type of connection to the main structure. For instance, the CT with dummy masses exhibited fundamental frequencies of 4.75 Hz in the X direction and 4.25 Hz in the Z direction, while the CT without dummy masses had fundamental frequencies of 11.75 Hz in the X direction and 8.25 Hz in the Z direction. Evidently, increasing the mass for the specimens led to a reduction in their fundamental frequencies.

In the Y direction, the pole connector with dummy masses specimens (CT, BCT) exhibited smaller fundamental frequency compared to the corresponding without dummy masses specimens. For example, the CT with dummy masses specimen had a fundamental frequency of 12.50 Hz, whereas the CT without dummy masses specimen had a fundamen-

Table 3
Test plan.

Step	Test	Direction	S_{DS} (g)	Scale factors (%)	Specimen under test	Remark
1	1	X	0.1	-	H-beam frame	Resonance test
			0.1	-	Ceiling	
	2	Y	0.1	-	H-beam frame	Resonance test
			0.1	-	Ceiling	
	3	Z	0.1	-	H-beam frame	Resonance test
			0.1	-	Ceiling	
	4	X,Y,Z	0.5	100	H-beam frame	Design level excitation
			0.5	100	Ceiling	
2	1	X	0.1	-	H-beam frame	Resonance test
			0.1	-	Ceiling	
	2	Y	0.1	-	H-beam frame	Resonance test
			0.1	-	Ceiling	
	3	Z	0.1	-	H-beam frame	Resonance test
			0.1	-	Ceiling	
	4	X,Y,Z	0.7	140	H-beam frame	Resonance test
			0.7	140	Ceiling	
3	1	X	0.1	-	Beam-column	Resonance test
			0.1	-	Wall	
	2	Y	0.1	-	Beam-column	Resonance test
			0.1	-	Wall	
	3	Z	0.1	-	Beam-column	Resonance test
			0.1	-	Wall	
	4	X,Y,Z	0.7	140	Beam-column	Resonance test
			0.7	140	Wall	

S_{DS} : Spectral response acceleration at short period.

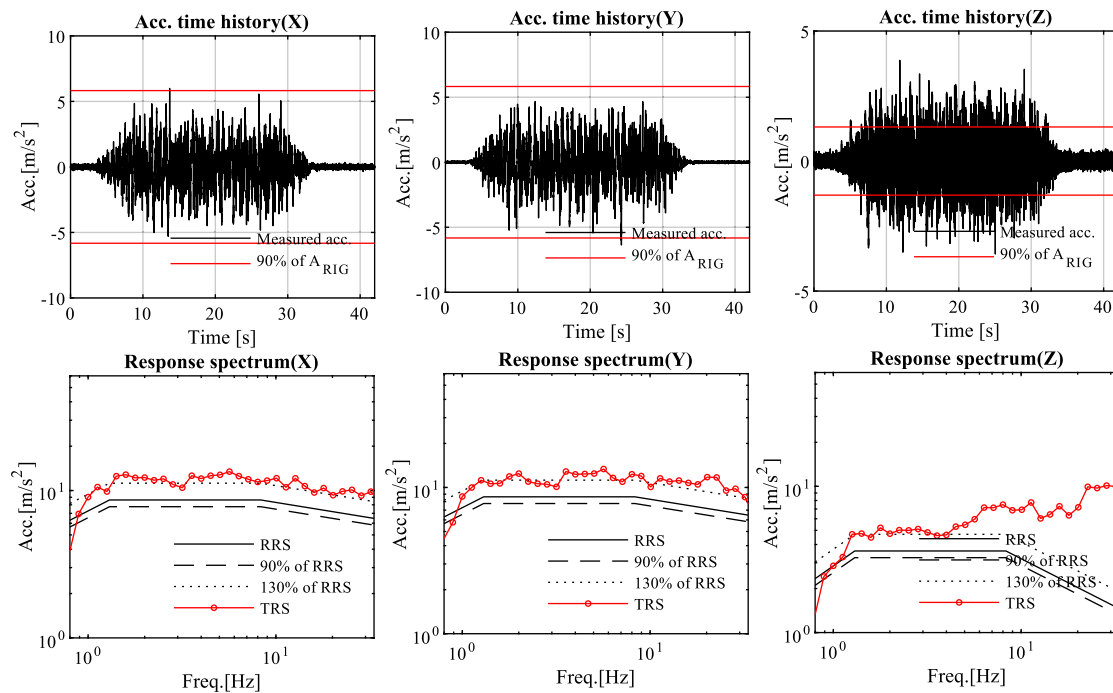


Fig. 10. Input acceleration time history corresponding to $S_{DS} = 0.5$ g, TRS, RRS, upper and lower matching limits (damping = 5%).

tal frequency of 19.75 Hz. In contrast, the direct connector specimens with dummy masses (HBT, WT) displayed larger fundamental frequencies. For instance, the HBT with dummy masses had a fundamental frequency of 26.00 Hz, while the H-beam frame without dummy masses type had a frequency of 19.75 Hz. This is believed to be due to the combined effect of the mass and stiffness of the dummy masses (with the stiffness in the Y direction of the dummy masses being the greatest, compared to the X and Z directions) and the stiffness of the pole connection in the Y direction.

In specimens augmented with dummy mass, the fundamental frequency values are significantly influenced by both the connection position to the frame and the pole's length. In the case of direct connector specimens with a dummy mass, the WT, being positioned higher than the HBT, demonstrated higher fundamental frequencies across the X, Y, and Z directions (X direction: 2.75 Hz vs. 2.25 Hz, Y direction: 30.75 Hz vs. 26 Hz, Z direction: 4.25 Hz vs. 4 Hz). Conversely, for pole connector specimens with dummy masses, the CT, featuring a longer pole, showed higher fundamental frequencies in the X and Z directions (X di-

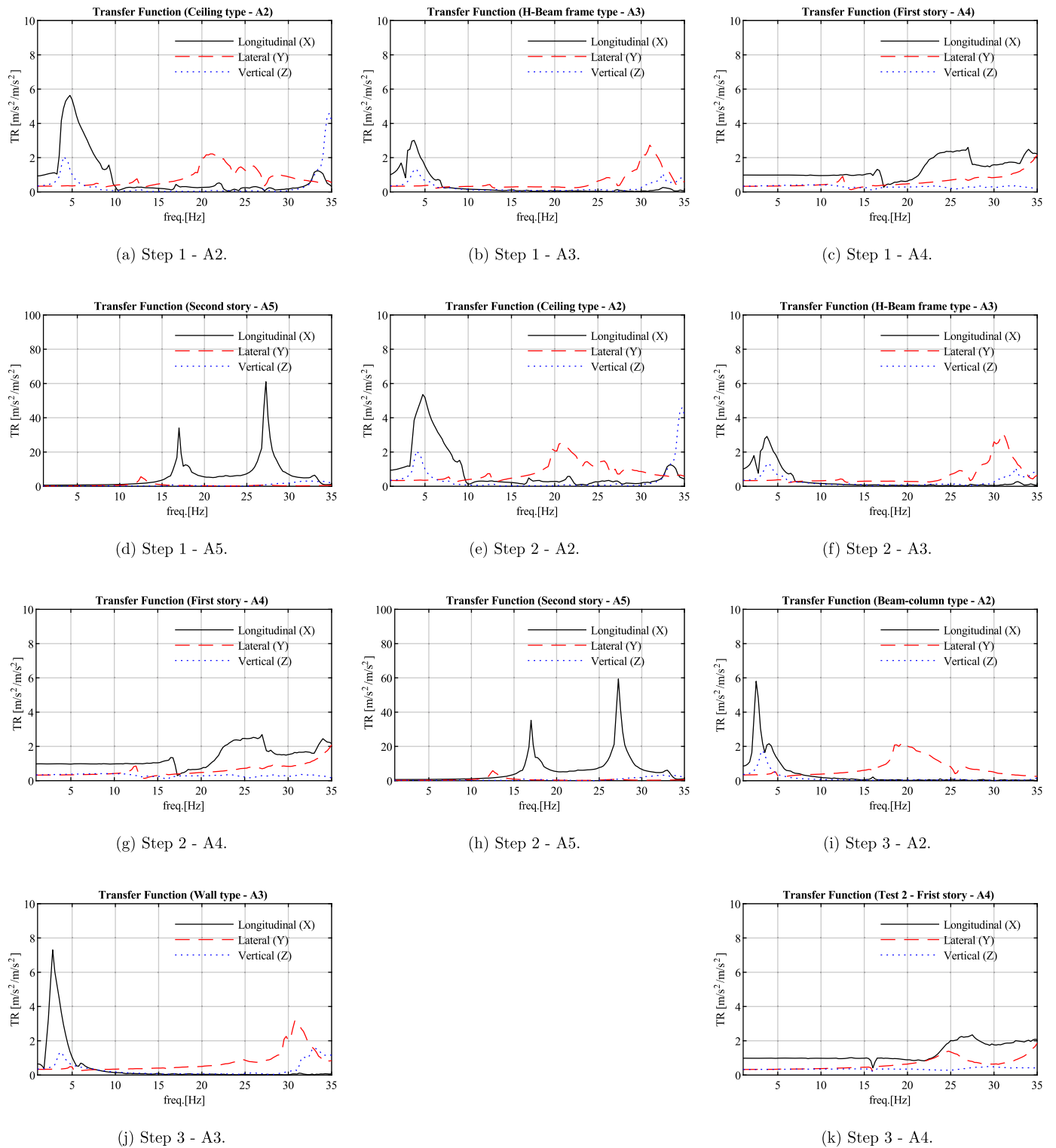


Fig. 11. The plot of the transfer function for Steps 1, 2, and 3 as obtained from the experimental data.

rection: 4.75 Hz vs. 2.25 Hz, Z direction: 4.25 Hz vs. 3.25 Hz), but a lower frequency in the Y axis (Y direction: 12.5 Hz vs. 30.75 Hz).

The frequency ratio r_f of the specimen with and without dummy masses is shown in Table 6.

Clearly, adding dummy mass resulted in a reduction of the r_f for all specimens in the X direction. In the Y direction, the addition of dummy mass increased r_f for direct connector specimens, HBT (r_f from 1.0 to 2.08) and WT (r_f from 1.00 to 1.24), while it decreased for pole con-

ductor specimens, BCT (r_f from 0.99 to 0.75), or remained unchanged ($r_f = 1.0$). The r_f in the Z direction could not be determined due to the absence of fundamental frequency data for the frame in this direction.

4.1.2. Numerical modal analysis

The acceleration responses obtained from the shaking table tests were first analyzed. Subsequently, the fundamental frequencies of the specimens were determined using the frequency domain transfer func-

Table 4
The fundamental frequency results of the specimens with dummy masses.

Step	Specimen	Location	Fundamental frequency results (Hz)			Remark
			X direction	Y direction	Z direction	
1	H-beam frame	A2	2.25	26.00	4.00	Fig. 11a
	Ceiling	A3	4.75	12.50	4.25	Fig. 11b
	Top of the column	A4	27.00	12.50	N/A	Fig. 11c
	Top of the T-beam	A5	17.00	12.50	16	Fig. 11d
2	H-beam frame	A2	2.25	26.00	4.00	Fig. 11e
	Ceiling	A3	4.75	12.50	4.25	Fig. 11f
	Top of the column	A4	27.00	12.50	N/A	Fig. 11g
	Top of the T-beam	A5	17.00	12.50	16.00	Fig. 11h
3	Beam-column	A2	2.50	18.50	3.25	Fig. 11e
	Wall	A3	2.75	30.75	4.25	Fig. 11f
	Top of the column	A4	27.50	24.75	N/A	Fig. 11g

Table 5
The fundamental frequencies - Test results of the specimens with and without dummy masses.

Specimen	Fundamental frequency - Test results (Hz)					
	X direction		Y direction		Z direction	
	WOD	WD	WOD	WD	WOD	WD
H-beam frame	13.50	2.25	19.75	26.00	8.00	4.00
Ceiling	11.75	4.75	19.75	12.50	8.25	4.25
Beam-column	12.25	2.50	19.25	18.50	8.00	3.25
Wall	14.00	2.75	19.50	30.75	9.25	4.25

Note: WD: With dummy masses; WOD: Without dummy masses.

Table 6
The fundamental frequency ratio r_f of the specimens with and without dummy masses.

Specimen	The fundamental frequency ratio r_f					
	X direction		Y direction		Z direction	
	WOD	WD	WOD	WD	WOD	WD
H-beam frame	0.55	0.08	1.00	2.08	N/A	N/A
Ceiling	0.47	0.28	1.00	1.00	N/A	N/A
Beam-column	0.51	0.09	0.99	0.75	N/A	N/A
Wall	0.58	0.10	1.00	1.24	N/A	N/A

Note: WD: With dummy masses; WOD: Without dummy masses.

tion technique. To verify these fundamental frequencies, modal analysis was performed using Mechanical Enterprise 2021/R1 [50].

Finite Element (FE) three-dimensional models were established to showcase the mechanical behavior of the specimens. Han et al. [51] developed the FE model for a pulley wireway system without dummy masses, as depicted in Fig. 12. The dimensions of the FE model were derived from the test specimen. All material properties (refer to Table 1 and Table 2), geometric and contact elements, were incorporated. The end base and connector were modeled using ANSYS's 3D 10-node elements (SOLID187) [52]. The cable and duct were modeled using CABLE280 and SHELL281, respectively.

For modal analysis, one hundred modes were defined. The first mode of natural vibration for the WT without a dummy mass was found in the Z-axis with a frequency of 9.25 Hz, as shown in Fig. 13(a). The second mode of natural vibration was observed in the X-axis with a frequency of 12.53 Hz, depicted in Fig. 13(b). Similarly, it can be stated that the third mode of natural vibration was 19.86 Hz in the Y-axis, illustrated in Fig. 13(c).

In Table 7, the fundamental frequencies derived from finite element analysis (FEA) for all specimens, both with and without dummy masses, are presented. Overall, comparing the results between test analysis and FEA indicates the reliability of the experimental outcomes. For the X and Z directions, the greatest difference between the fundamental frequency results in experiments and FEA is just 1.77 Hz. In the Y

Table 7
The fundamental frequency - FE analysis results of the specimens with and without dummy masses.

Specimen	Fundamental frequencies - FEA results (Hz)					
	X direction		Y direction		Z direction	
	WOD	WD	WOD	WD	WOD	WD
H-beam frame	12.53	3.17	19.86	35.39	9.25	2.90
Ceiling	10.34	4.04	18.07	12.42	8.52	3.60
Beam-column	10.67	4.27	18.09	17.90	8.60	3.59
Wall	12.53	3.17	19.86	35.39	9.25	2.90

Note: WD: With dummy masses; WOD: Without dummy masses.

direction, the discrepancy is very small for both CT and BCT; however, it is relatively larger for WT and HBT. This can be attributed to the challenges in accurately simulating the combined effect of the mass and stiffness of the dummy masses in the direct connector specimens.

4.1.3. The frequency content of the input motion and the system's fundamental frequencies

The input ground motion for the shaking table should be a non-stationary broadband random excitation signal, providing at least 20 seconds of strong motion, and typically lasting around 30 seconds in total duration. It includes frequency contents ranging from 1.3 Hz to 33.3 Hz, as shown in Fig. 9 and Fig. 10. This frequency range spans all the fundamental frequencies of the lighting system assessed in this study, which are between 2.25 Hz and 30.75 Hz.

In accordance with AC156, the study identified that the maximum spectral acceleration in the low-frequency content range, which is below 10 Hz and specifically falls between 1.3 Hz to 8.3 Hz, occurred in the X and Y directions. In contrast, for the Z direction, the maximum spectral acceleration was observed within a wider range, extending from 1.3 Hz to 33.33 Hz.

The changes in the fundamental frequency affect the seismic response of the system. With the incorporation of a dummy mass, the fundamental frequency in the X direction decreased from the range of approximately 11.75 to 13.5 Hz, which is outside the maximum spectral acceleration range of 1.3 Hz to 8.3 Hz, down to a range of 2.25 Hz to 4.75 Hz. In the Y direction, the change in fundamental frequency from about 19.25 Hz to 19.75 Hz to the range of 12.5 Hz to 30.75 Hz still falls outside the range of maximum spectral acceleration. In the Z direction, the shift in fundamental frequency from approximately 8.0 Hz to 9.25 Hz to the range of 3.25 Hz to 4.25 Hz is within the range of maximum spectral acceleration.

4.2. Visual inspection

All specimens, regardless of being with or without dummy masses, were visually inspected pre- and post-shaking table tests to identify potential deformations or damage. The evaluations showed:

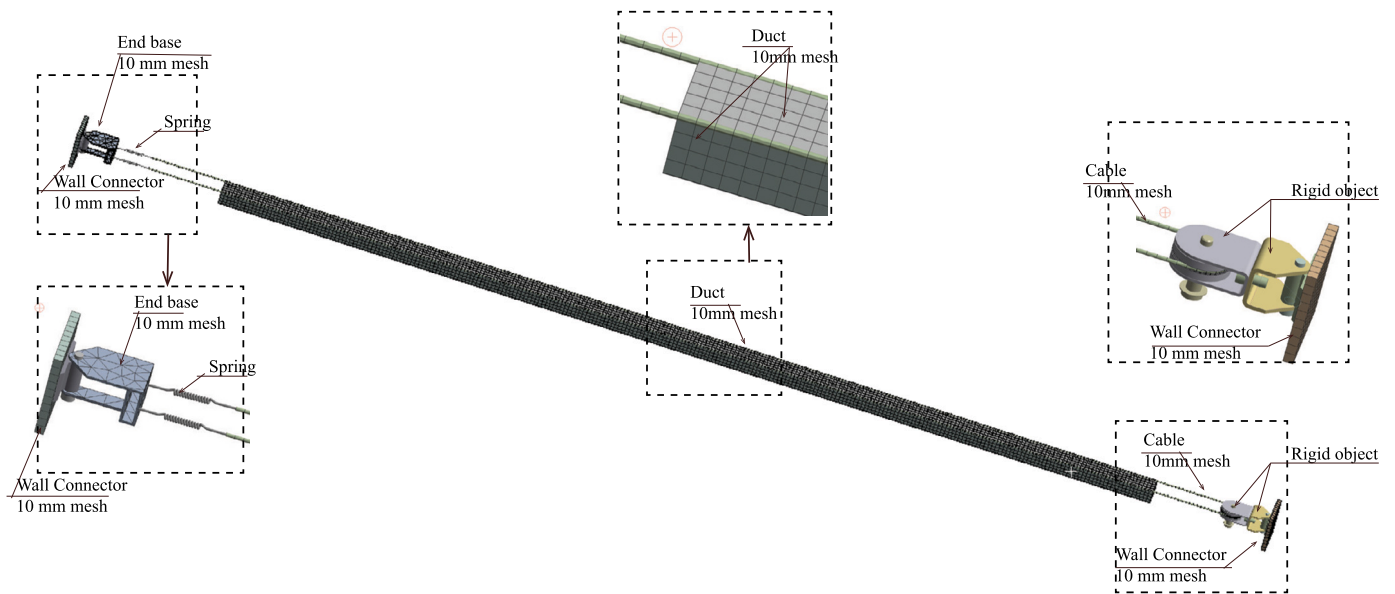


Fig. 12. The FE model for WT without dummy mass in ANSYS.

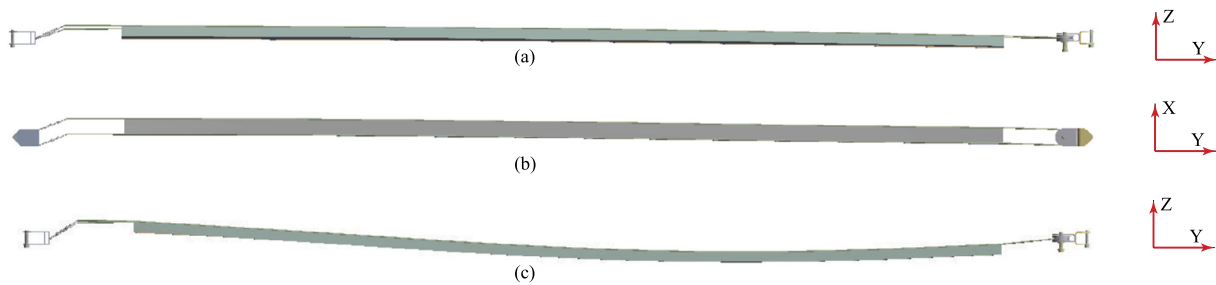


Fig. 13. The first three mode shapes of the WT without dummy masses: (a) Mode 1 in Z direction ($f = 9.24$ Hz); (b) Mode 2 in X direction ($f = 12.53$ Hz); (c) Mode 3 in Y direction ($f = 19.86$ Hz).

- Absence of significant structural anomalies or apparent damages at bolt connections and connectors for both specimens with and without dummy masses [40].
- No instances of toppling or collapse in any of the specimens.
- Continued full operability of the lighting system throughout the tests.

These observations validate the robustness and efficiency of the wireway vibration attenuation system under seismic influences and various mass conditions, aligning with the stipulations of ICC-ES AC156 and SPS-F KOCED 0007-7419:2021 [41,47].

4.3. Evaluating the effect of the masses of lighting systems on seismic performance

4.3.1. Displacement response

During the tests, LVDTs D1 and D2 captured lateral displacements (X direction) of all four specimens. Fig. 14 shows the response lateral displacement time history plots for the specimens with dummy masses. It is clear that the fundamental frequency r_f influenced the maximum lateral displacement.

- When subjected to an earthquake magnitude of $S_{ds} = 1.0g$, all specimens without dummy mass displayed similar lateral displacements [40].
- When subjected to earthquake magnitudes of $S_{ds} = 0.5g$ and $S_{ds} = 0.7g$, specimens with dummy mass exhibited response-time histories of lateral displacement, as illustrated in Fig. 14. The data

revealed a direct correlation between the earthquake magnitude and the specimens' maximum relative displacement. Notably, specimens with dummy masses employing pole connectors (see Table 6) demonstrated the larger lateral displacements in comparison to those with direct connectors.

As per standards from the Korean National Radio Research Agency [53], top equipment displacement should not breach the 75 mm mark for ensuring the integrity of adjacent NSCs. The HBT specimen adhered to this criterion. Conversely, CT, BCT, and WT specimens exhibited displacements that went beyond the recommended 75 mm limit during certain phases of the tests.

4.3.2. Acceleration response

The acceleration response of the novel system, influenced by the frequency ratio r_f , was explored using four specimens. These specimens, without dummy masses [40] and with dummy masses, were tested on a shaking table. Fig. 15 and Fig. 16 show the response acceleration time history plots for Steps 1-3 of the specimens with dummy masses.

- In experiments where specimens without additional masses were subjected to a $S_{DS} = 1.0g$ earthquake, distinct behaviors emerged based on the type of connectors used. Specimens with direct connectors demonstrated higher r_f in the X direction, ranging from 0.55 to 0.58, compared to those with pole connectors, whose r_f ranged from 0.47 to 0.51. As a result, the direct connector specimens exhibited lower acceleration responses in the X direction. In the Y direction, despite the frequency ratios of all specimens

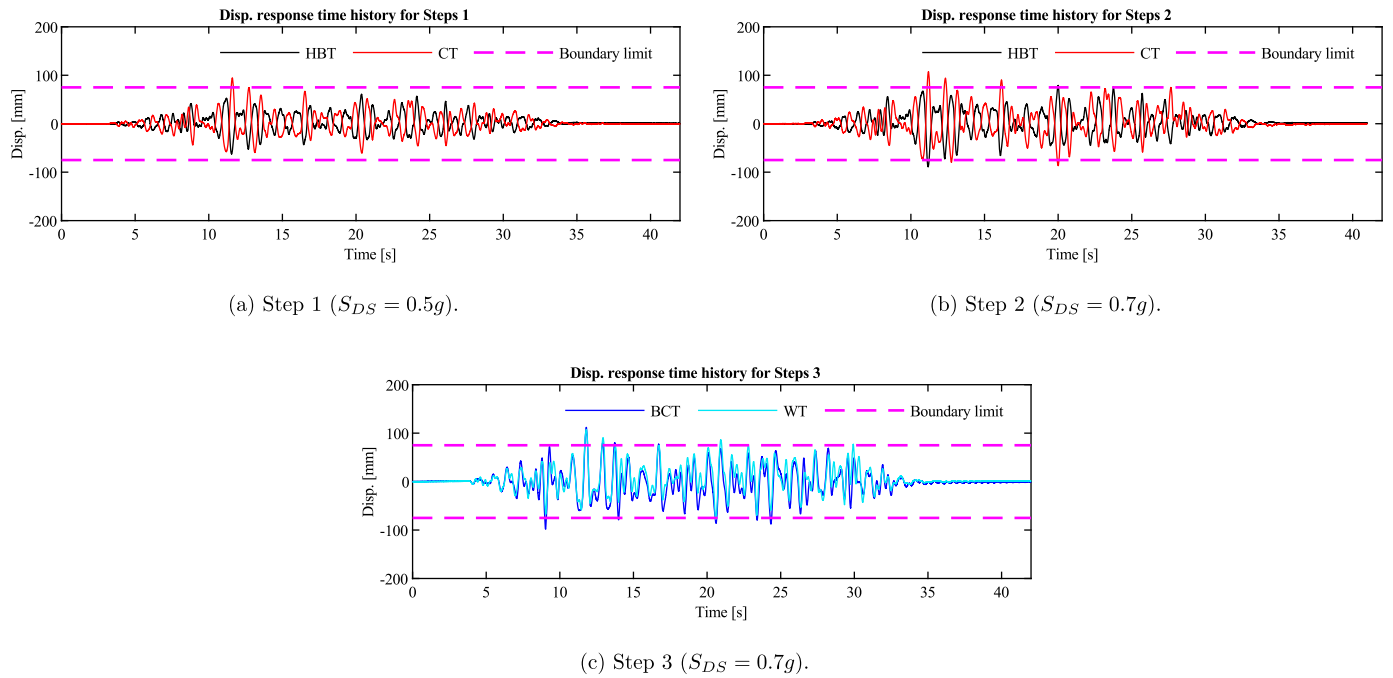


Fig. 14. The lateral displacement time history plots for the specimens with dummy masses.

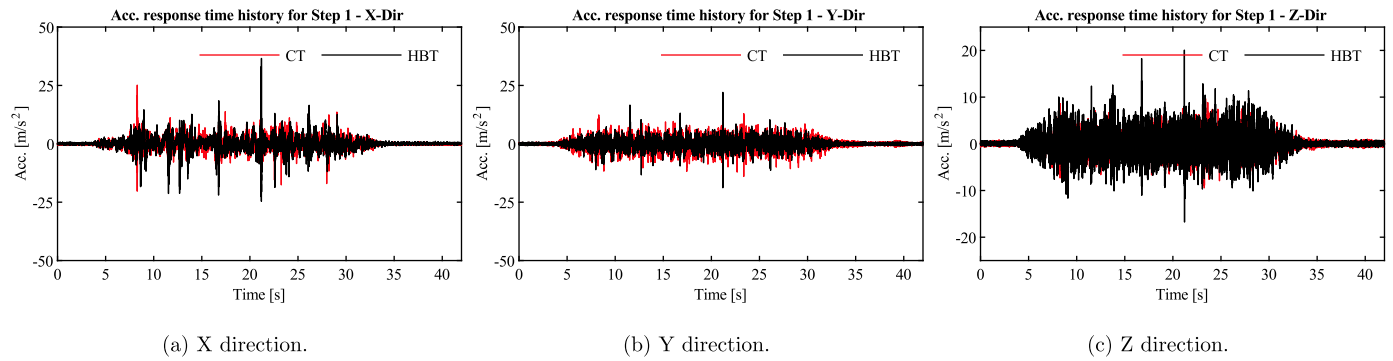


Fig. 15. The response acceleration time history plots of specimens with dummy masses for Step 1 ($S_{DS} = 0.5g$).

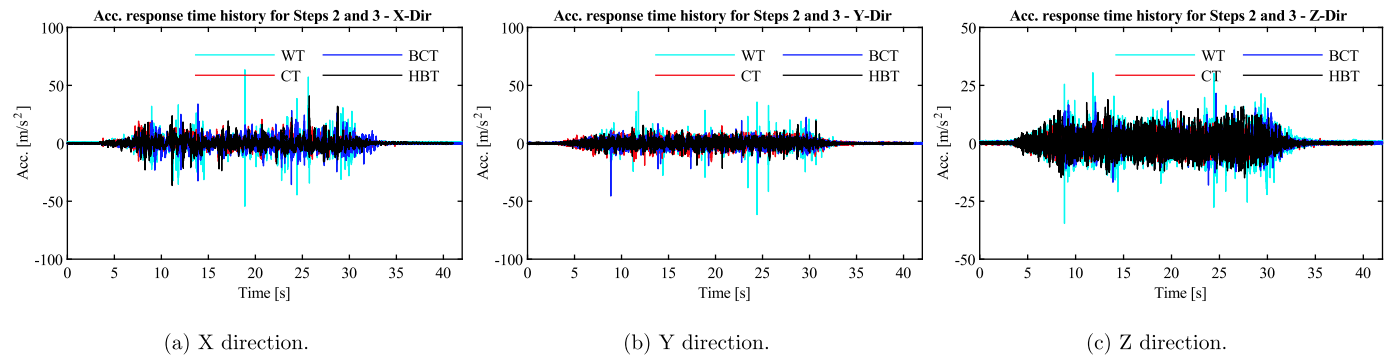


Fig. 16. The response acceleration time history plots of specimens with dummy masses for Steps 2 and 3 ($S_{DS} = 0.7g$).

being nearly identical, those with direct connectors still showed smaller acceleration responses than the pole connector specimens. Although the r_f in the Z direction was indeterminable, the fundamental frequencies for both connector types in this direction were similar. Nonetheless, the direct connector specimens consistently displayed smaller acceleration responses in the Z direction than those with pole connectors.

- For the specimens with dummy masses:
 - A diminished acceleration response was identified in the pole connector type specimens when dummy masses were introduced, compared to the direct connector type specimens. The acceleration response among the specimens became more stable.
 - In Fig. 15, under a $S_{DS} = 0.5$ g earthquake, the specimens demonstrated a consistent acceleration response. The HBT specimen, which is a direct connector type with a frequency ratio (r_f) of 0.08, exhibited greater acceleration responses in the X direction compared to the CT specimen with an r_f of 0.28. In contrast, in the Y direction, the HBT specimen with an r_f of 2.08 showed reduced acceleration response relative to the CT specimen with an r_f of 1.00. This indicates that a lower r_f results in higher acceleration responses in the specimens. Although the r_f in the Z direction was indeterminate, the fundamental frequencies for both types of specimens in this direction were found to be similar. However, the HBT specimen continued to display larger acceleration responses in the Z direction.
 - In Fig. 16, for a $S_{DS} = 0.7$ g earthquake, CT specimens with the highest r_f (0.28) had the lowest acceleration in the X direction, while the HBT specimen with the highest r_f (2.08) showed the lowest acceleration in the Y direction. r_f in the Z direction was undetermined. Pole connector specimens with a higher fundamental frequency (4.25 Hz vs. BCT's 3.25 Hz) in Z direction had smaller acceleration responses. Direct connector specimens like WT with a higher frequency (4.25 Hz) compared to HBT (4.00 Hz) also showed higher acceleration responses in Z direction.
 - Significantly, when compared to the CT specimen without dummy masses, which had a r_f of 1.00 and a fundamental frequency of 19.75 Hz in the Y direction, the CT specimen with dummy mass exhibited an r_f of 1.00 and a fundamental frequency of 12.5 Hz. Notably, this did not result in an abrupt increase in acceleration response in the Y direction. Therefore, a decrease in the fundamental frequency led to a notably stable acceleration response in specimens with long poles.

4.3.3. Peak resonant oscillation

The behavior of the specimens needs to be carefully considered when resonance occurs during earthquakes. Therefore, a comprehensive and detailed investigation was performed in the frequency domain.

The acceleration spectral density (ASD) presents the distribution of acceleration response for each frequency recorded during the shaking table experiment. To calculate the ASD functions from the collected data, Welch's method is employed. This method, introduced by Welch and Solomon [54,55], involves analyzing windowed and zero-padded frames from the signal, denoted as the m^{th} segment of the signal x :

$$x_m(n) \triangleq \omega(n) x(n + mR) \quad (7)$$

$$n = 0, 1, \dots, M - 1; m = 0, 1, \dots, K - 1$$

Where R is defined as the window hop size and let K denote the number of available frames (or segments). The window function denotes as $\omega(n)$. M denotes number of points in each segment. Then, the periodogram $P_{x_m, M}(\omega_k)$ of the m^{th} segment is given by:

$$P_{x_m, M}(\omega_k) = \frac{1}{M} \left| \text{FFT}_{N, k}(x_m) \right|^2 \triangleq \frac{1}{M} \left| \sum_{n=0}^{N-1} x_m(n) e^{-j2\pi nk/N} \right|^2 \quad (8)$$

Table 8

The maximum ASD value of the specimens with dummy masses.

Step	Specimen	z (m)	S_{DS} (g)	Peak ASD (G^2/Hz)		
				X-dir	Y-dir	Z-dir
1	Ceiling	2.430	0.500	0.012	0.013	0.010
	H-beam frame	0.505	0.500	0.018	0.006	0.029
2	Ceiling	2.430	0.700	0.018	0.017	0.014
	H-beam frame	0.505	0.700	0.037	0.009	0.043
3	Beam-column	1.070	0.700	0.131	0.009	0.037
	Wall	1.070	0.700	0.108	0.010	0.043

Where FFT denotes the Fast Fourier transform algorithm. The Welch estimate of the power spectral density $\hat{S}_x^w(\omega_k)$ is as follows (an average of periodograms across time):

$$\hat{S}_x^w(\omega_k) \triangleq \frac{1}{K} \sum_{m=0}^{K-1} P_{x_m, M}(\omega_k) \quad (9)$$

In this study, the ASD plots were generated using the pwelch function in MATLAB [56]. The displayed ASD values range from 1 Hz to 256 Hz. The ASD calculations employed the following parameters: $M = 1024$ points per segment, $K = 21$ segments with 50% duplicates ($S = 0.5M$), a time per segment of 2 seconds, and a frequency resolution (df) of 0.5 Hz.

The effects of the fundamental frequency ratio, r_f , on the ASD of the novel system were investigated using eight specimens. This study involved four specimens without additional dummy masses, as referenced in [40], and four specimens with dummy masses, all of which were tested using a shaking table.

Fig. 17 shows the acceleration spectral density (ASD) plots for the specimens without dummy masses.

The peak ASD values when resonance occurred and the corresponding frequencies of the four specimens with dummy masses during Steps 1-3 are shown in Table 8. Fig. 18 displays the ASD plots for the CT (pole connector) and HBT (direct connector) specimens with dummy mass in the X, Y, and Z directions during Step 1 ($S_{DS} = 0.5$ g) and Step 2 ($S_{DS} = 0.7$ g), respectively.

Fig. 19 displays ASD plots for the specimens with dummy masses in the X, Y, and Z directions during Steps 2 and 3 ($S_{DS} = 0.7$ g).

- For specimens without dummy masses:
 - When subjected to an earthquake of $S_{DS} = 1.0$ g [40]:
 - * Direct connectors had higher frequency ratios (r_f : 0.55-0.58) in the X direction than pole connectors (r_f : 0.47-0.51), leading to lower X-direction peak ASD. Despite similar r_f values in the Y direction, direct connectors exhibited smaller peak ASDs compared to pole connectors. In the Z direction, while r_f values were indeterminable, fundamental frequencies were similar across connector types. However, direct connectors consistently showed smaller peak ASDs in the Z direction.
 - * The CT specimen with a longer pole demonstrated a substantially higher peak ASD value in the Y direction, greatly exceeding the values of other models, with an increase ranging from 89 to 584 times. As a result, for specimens without dummy mass, those with long poles are not recommended.
- For specimens with dummy masses:
 - Analysis during earthquakes with magnitudes $S_{DS} = 0.5$ g (see Fig. 18) and $S_{DS} = 0.7$ g (see Fig. 19):
 - * In the pole connector type specimens, a reduction in peak ASD values was observed upon the introduction of dummy masses, as compared to the direct connector type specimens. Intriguingly, the CT specimen did not manifest any sharp surges in its peak ASD value.
 - * The HBT specimen, which is a direct connector type with a r_f of 0.08, showed greater peak ASD values in the X direction

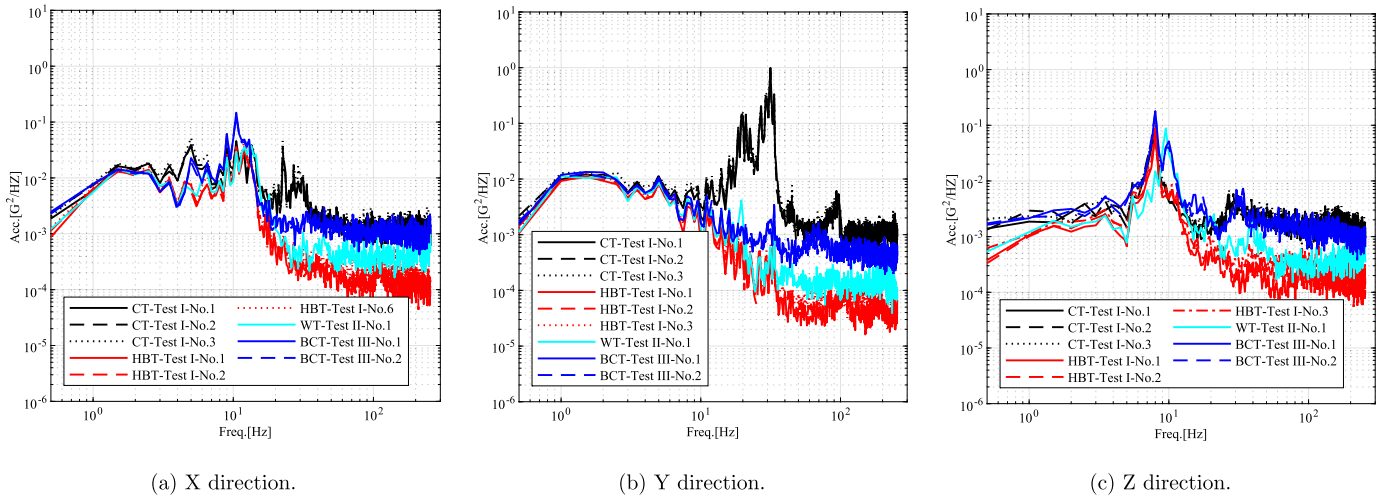


Fig. 17. ASD plots of the four specimens without dummy mass ($S_{DS} = 1.0g$) [40].

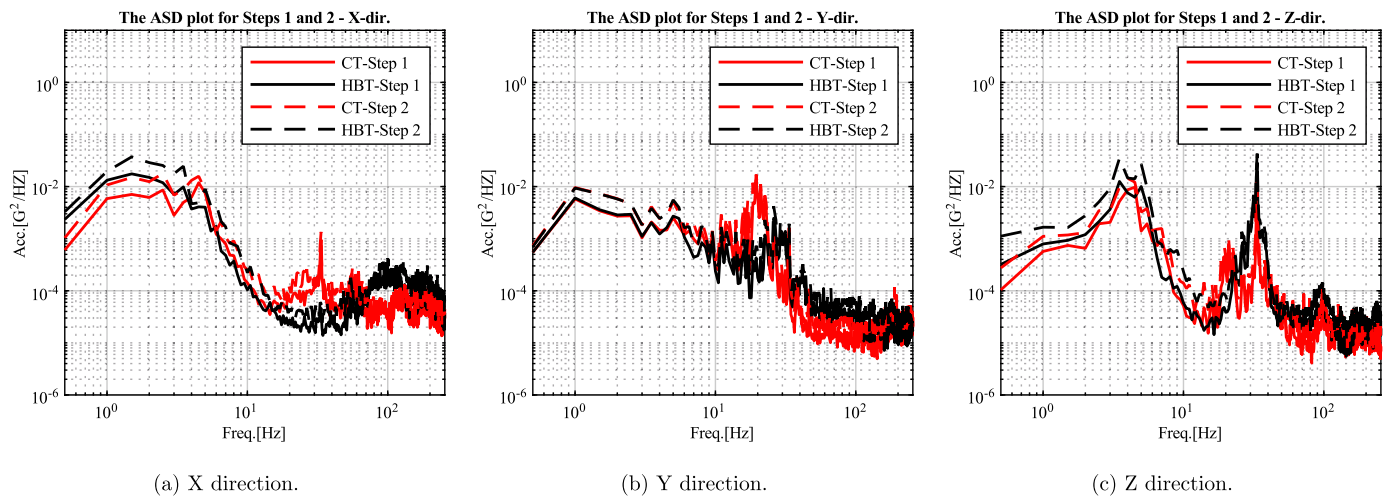


Fig. 18. ASD plots of the Step 1 ($S_{DS} = 0.5g$) and Step 2 $S_{DS} = 0.7g$) for the specimens with dummy masses.

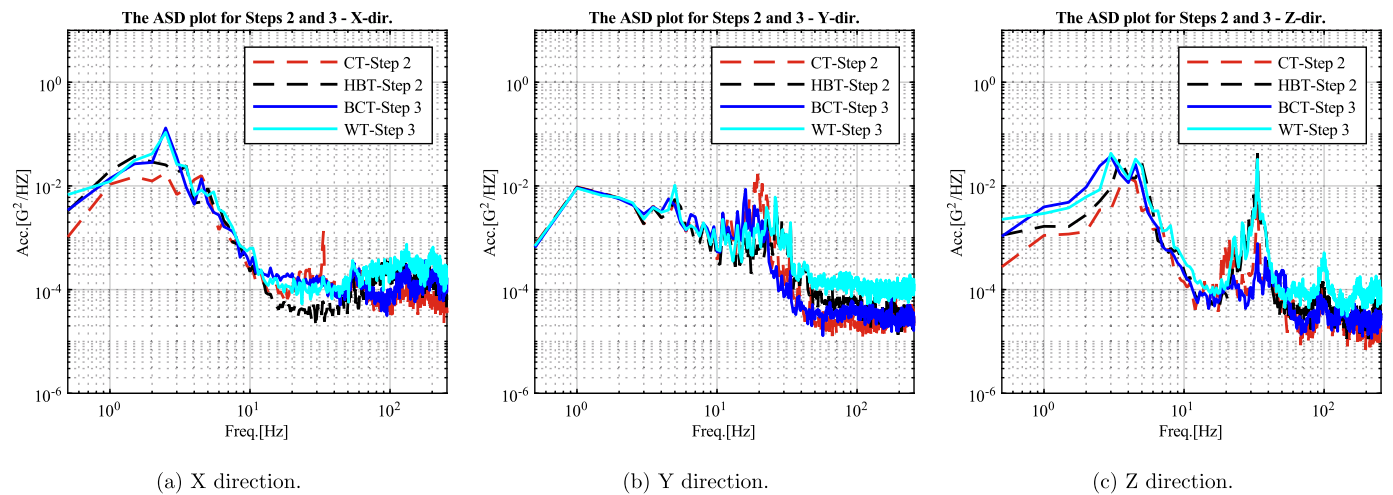


Fig. 19. ASD plots of the Steps 2 and 3 ($S_{DS} = 0.7g$) for the specimens with dummy masses.

compared to the CT specimen with an r_f of 0.28. Although the r_f in the Z direction was indeterminate, the fundamental frequencies for both specimen types in this direction were similar. Nonetheless, the HBT specimen continued to exhibit larger peak in the Z direction. Specifically:

- For $S_{DS} = 0.5g$, CT's decrease in peak ASD values was 32.40% (X direction) and 66.21% (Z direction) compared to HBT.
- For $S_{DS} = 0.7g$, CT showed a reduction in peak ASD values by 52.04% (X direction) and 66.43% (Z direction) relative to HBT.

* In the Y direction, the HBT specimen with an r_f of 2.08 had a lower peak ASD than the CT specimen with an r_f of 1.00, indicating that lower r_f results in higher peak ASD. The CT specimen's peak ASD values were higher than HBT's by 121.17% for $S_{DS} = 0.5 g$ and 81.94% for $S_{DS} = 0.7 g$.

* Compared to the CT specimen without dummy mass, which had the r_f of 1.00 and a fundamental frequency of 19.75 Hz in the Y direction, the CT specimen with dummy mass, possessing a similar r_f of 1.00 but a lower fundamental frequency of 12.5 Hz, exhibited no significant increase in peak ASD in the Y direction. This suggests that a reduced fundamental frequency in long pole specimens contributes to stabilizing the specimen's oscillation during resonance.

– For pole connector specimens:

* Fig. 19a-c show that the CT specimen with an r_f of 1.00 in the Y direction showed an 85.75% increase in peak ASD compared to the BCT specimen's r_f of 0.75. Conversely, the CT specimen with an r_f of 0.28 in the X direction exhibited an 86.38% reduction in peak ASD relative to the BCT specimen with an r_f of 0.09.

* Previous study showed that in the Y direction, CT specimens with long pole and without dummy mass needed attention due to their high peak ASD. Although the CT specimen with dummy masses had the r_f , its peak ASD remained greater than that of the BCT specimen, despite a significant reduction in their difference compared to cases without dummy mass. This highlights the critical role of pole length in earthquake performance of the pole connector specimens, emphasizing the importance of reducing pole length to control Y-direction oscillations.

• For direct connector specimens (observations from Fig. 19a-c during $S_{DS} = 0.7g$):

- The peak ASD value increased as the frequency ratio (r_f) decreased. In the Y direction, the WT specimen, with an r_f of 1.24, exhibited peak ASD values that were 9.93% higher compared to the HBT specimen, which had an r_f of 2.08 in the Y direction.
- Peak ASD value increased with elevation in mounting position. The WT specimen, mounted at $z = 1.070 m$, demonstrated peak ASD values higher by 189.74% in the X direction compared to the HBT specimen, which was mounted at $z = 0.505 m$, when the r_f of the two specimens was nearly the same in this direction.
- Interestingly, when the fundamental frequencies of the HBT and WT specimens were the same, the peak ASD value in the Z direction was observed to be similar for both specimens.

4.3.4. Earthquake energy dissipation

The root mean square acceleration (GRMS) [57] is a measure of the energy accumulated in a structure as a result of an earthquake. In the frequency domain, the GRMS is defined as the square root of the area under the ASD curve. The area under the ASD curve of the j^{th} frequency segment (a_j) between the frequencies f_{i-1} and f_i corresponds to P_{i-1} and P_i [57,58].

Table 9

Overall GRMS value of the specimens with dummy masses.

Step	Specimen	z (m)	S_{DS} (g)	Overall GRMS (g)			
				X-dir	Y-dir	Z-dir	Total
1	Ceiling	2.430	0.500	0.214	0.238	0.169	0.621
	H-beam frame	0.505	0.500	0.254	0.188	0.261	0.703
2	Ceiling	2.430	0.700	0.282	0.299	0.223	0.803
	H-beam frame	0.505	0.700	0.354	0.248	0.354	0.956
3	Beam-column	1.070	0.700	0.400	0.254	0.294	0.947
	Wall	1.070	0.700	0.445	0.297	0.398	1.139

m is the slope of the segment j between the frequencies f_{i-1} and f_i :

$$m = 10 \log \left(\frac{P_i}{P_{i-1}} \right) \frac{\log(2)}{\log \left(\frac{f_i}{f_{i-1}} \right)} \tag{10}$$

for $m \neq -10 \log(2)$:

$$a_{f_i,j} = 10 \log(2) \frac{P_i}{10 \log(2) + m} \left[f_i - f_{i-1} \left(\frac{f_{i-1}}{f_i} \right)^{m/10 \log(2)} \right] \tag{11}$$

for $m = -10 \log(2)$:

$$a_{f_i,j} = P_{i-1} f_{i-1} \ln \left(\frac{f_i}{f_{i-1}} \right) \tag{12}$$

The GRMS value at the j^{th} frequency segment:

$$GRMS_j = \sqrt{a_j} \tag{13}$$

The overall GRMS level at j^{th} at frequency f_i is then:

$$GRMS_{f_i} = \sum_{m=0}^j a_m \tag{14}$$

The overall GRMS is the value at the end of the Cumulative acceleration root mean square (CRMS) plots. In the absence of dummy masses, the seismic energy was analyzed for different specimens, as shown in Fig. 20 [40].

The Overall GRMS of the four specimens with dummy mass during Steps 1-3 are shown in Table 9.

Fig. 21 and Fig. 22 present cumulative acceleration root mean square plots for four specimens with dummy masses in the X, Y, and Z directions during Steps 1-3.

Clearly, for the novel lighting support system, particularly in systems with pole connectors, adjusting the system's fundamental frequency downwards by adding dummy mass has effectively mitigated the potential amplification of the structural response due to high-frequency ground motion [59].

• In the absence of dummy masses, seismic energy was analyzed for different specimens, as presented in Fig. 20 [40].

- In $S_{DS} = 1.0 g$ earthquake tests, specimens with direct connectors had higher r_f in the X direction (from 0.55 to 0.58) compared to pole connectors (r_f from 0.47 to 0.51), leading to lower earthquake energy in the X direction. Despite similar r_f values in the Y direction, direct connectors exhibited lower earthquake energy than pole connectors. In the Z direction, although r_f values could not be determined, both connector types had similar fundamental frequencies, but direct connectors consistently showed lower earthquake energy in the Z direction.

– The CT specimen, with a 2.15 m pole length and $r_f = 1.00$, exhibited notably higher earthquake energy in the Y direction than the HBT, WT, and BCT specimens, highlighting the disadvantages of long pole connectors.

• For specimens with dummy masses, the introduction of a dummy mass was observed to generally result in lower seismic energy

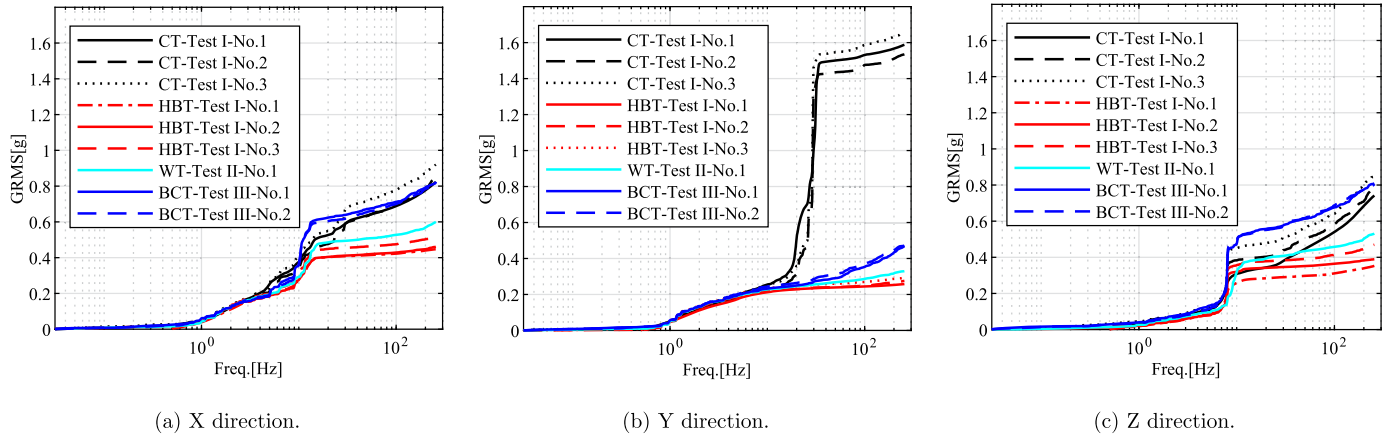


Fig. 20. CRMS plots of the specimens without dummy mass ($S_{DS} = 1.0$ g) [40].

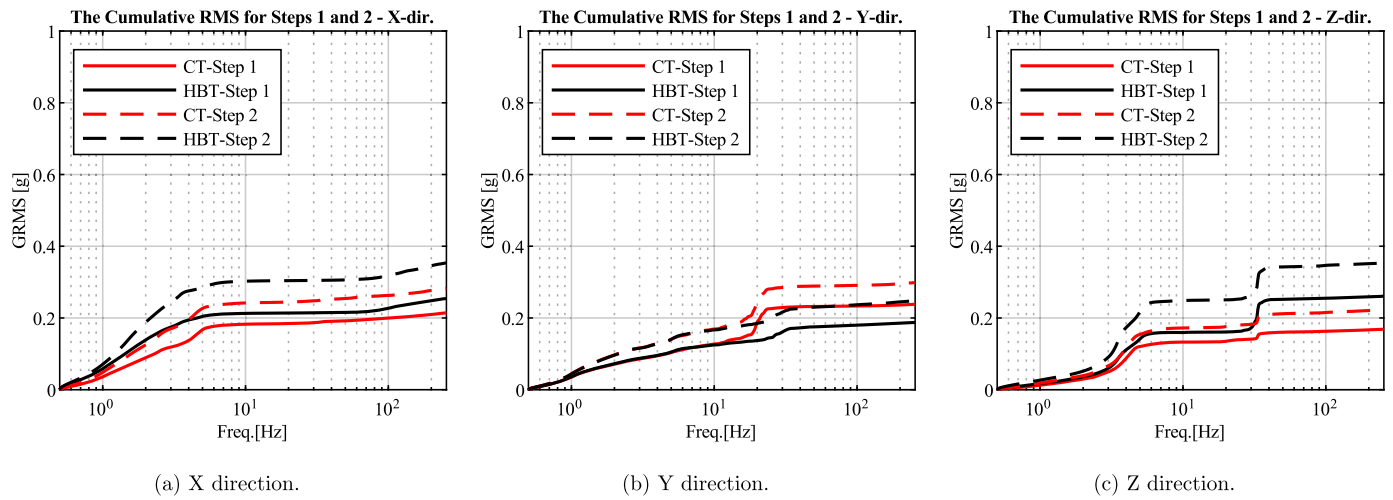


Fig. 21. CRMS plots of the specimens with dummy masses for Steps 1 ($S_{DS} = 0.5$ g) and 2 ($S_{DS} = 0.7$ g).

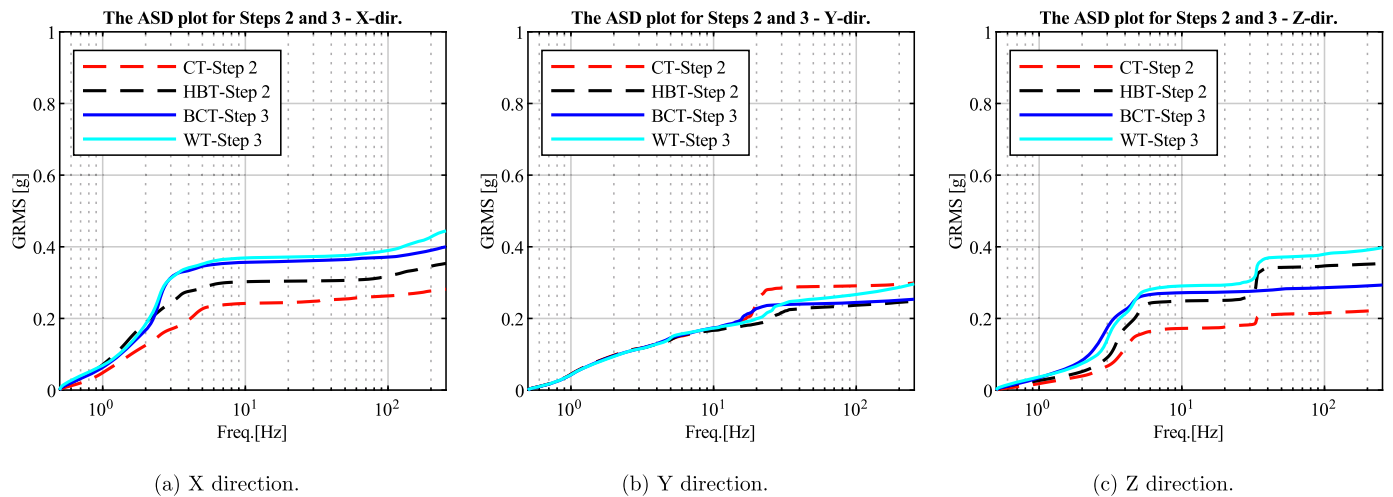


Fig. 22. CRMS plots of the specimens with dummy masses for Steps 2 and 3 ($S_{DS} = 0.7$ g).

for specimens with pole connectors compared to those with direct connectors. The overall GRMS value of pole connector specimens decreased by 0.94% to 29.46% across the X, Y, and Z directions in comparison to direct connector specimens. Notably, the CT specimen showed no significant surge in earthquake energy values around its resonant frequency.

- As visualized in Fig. 21, a direct proportionality between the earthquake energy of the specimens and earthquake magnitude was observed. During seismic events with magnitudes $S_{DS} = 0.5g$ and $S_{DS} = 0.7g$:
 - * Under earthquakes of ($S_{DS} = 0.5 g$ and $S_{DS} = 0.7 g$), the HBT specimen, a direct connector type with r_f of 0.08, displayed a higher overall GRMS in the X direction by 15.69% and 35.35%, respectively, compared to the CT specimen with an r_f of 0.28. In the Y direction, however, the HBT specimen with an r_f of 2.08 had a lower overall GRMS by 26.94% and 20.34% than the CT specimen with an r_f of 1.00. Although the r_f in the Z direction was indeterminate, the fundamental frequencies were similar for both specimen types. Yet, the HBT specimen consistently showed larger overall GRMS in the Z direction by 20.25% and 37.07% for each seismic intensity. This suggests that a lower r_f correlates with higher overall GRMS in the specimens.
- An observation made during the $S_{DS} = 0.7 g$ seismic event, as shown in Fig. 22, highlighted:
 - * For direct connector specimens: the overall GRMS value increased as the r_f decreased. Specifically, in the Y direction, the WT specimen with an r_f of 1.24 exhibited overall GRMS values that were 12.31% higher than those of the HBT specimen, which had an r_f of 2.08.
 - * For direct connector specimens: the overall GRMS value increased with the elevation of the mounting position. The WT specimen, mounted at $z = 1.070 m$, demonstrated overall values that were 25.77% higher in the X direction and 12.31% in the Z direction compared to the HBT specimen, which was mounted at $z = 0.505 m$, when the r_f in the X direction and the fundamental frequency in the Z direction of the two specimens were nearly the same.
 - * In pole connector specimens, the study found that CT specimens with long poles and without dummy mass showed an overall GRMS 3.38 times higher than that of BCT specimens in the Y direction [40]. Even with a larger r_f of 1.00 compared to the BCT's 0.75 when using dummy masses, the CT specimen's overall GRMS was still 17.73% higher than the BCT specimen's one. This emphasizes the significant role of pole length in the earthquake performance of these specimens and the need to reduce pole length for better performance in the Y direction.
 - * For pole connector specimens: while the fundamental frequencies of the two specimens in the Z direction were nearly the same, the CT specimen in the Z direction exhibited a 24.09% reduction in overall GRMS relative to the BCT specimen.
 - * In the case of pole connector specimens, the CT specimen, with a higher r_f of 0.28 in the X direction, exhibited a 29.45% reduction in overall GRMS compared to the BCT specimen, which had a lower r_f of 0.09.

5. Conclusions

Through tri-axial shaking table tests, the seismic behavior of a wireway vibration attenuation system for exposed raceway light fixtures was examined. Eight prototypes, differing in connectors and mass, were studied. Input motion was based on the ICC-ES AC156. Key conclusions are:

- A series of shaking table tests that met the AC156 standard were conducted, and they proved that the pulley wireway system would perform efficiently during earthquakes.
- The mass and stiffness of dummy masses critically influence the fundamental frequencies of a novel structural system, with specimens having dummy masses displaying lower frequencies in the X and Z directions. In contrast, in the Y direction, the frequency varied with connector type and the presence of dummy masses, where pole connectors with dummy masses showed lower frequencies, and direct connectors exhibited higher frequencies.
- In specimens with dummy mass, fundamental frequencies were influenced by the connection's position to the frame and the pole's length, with higher or longer poles resulting in increased frequencies in certain directions.
- Adding mass changed the fundamental frequency ratio of the lighting system relative to the main structure: it decreased the ratio in the X direction, increased it for direct connectors, and either reduced or maintained it for pole connectors in the Y direction.
- Specimens without dummy masses showed consistent maximum lateral displacements. In contrast, adding masses to the system resulted in pole connectors exhibiting greater lateral displacements than those with direct connectors.
- Without a dummy mass, direct connector specimens outperformed pole connectors. For specimens with dummy masses, introducing a dummy mass generally led to lower seismic energy in pole connector specimens than in direct connector specimens. The overall GRMS value in pole connector specimens decreased by 0.94% to 29.46% across the X, Y, and Z directions compared to direct connector specimens.
- The introduction of dummy masses significantly stabilized acceleration in specimens, with the most notable effect in the long pole connector specimen, where it substantially reduced abrupt acceleration, peak oscillation and earthquake energy. Lower fundamental frequency ratios between the novel system and main structure resulted in increased acceleration, peak oscillation and earthquake energy in the X and Y directions. In the Z direction, direct connectors with dummy masses showed higher acceleration, peak oscillation and earthquake energy compared to pole connectors, but in the absence of dummy masses, this trend was reversed.
- For the novel lighting system, with or without dummy mass, the earthquake energy of direct connector specimens increased with the elevation of the mounting position. For pole connector systems, this underscores the critical role of pole length in earthquake performance and the necessity of reducing pole length for improved Y-direction performance.

Overall, this study enhances the understanding of wireway vibration attenuation systems for exposed raceway light fixtures in seismic environments. It underscores the significance of selecting appropriate connectors, the positioning connected to main structures, and considering the mass of the lighting system. Future research using full-scale specimens, spanning a length of 25 meters, is anticipated to offer further insights into the system's seismic performance.

The earthquake-resistant design standards for NSCs remain limited. This study's findings have the potential to enhance current provisions regarding NSCs. Specifically, it emphasizes the crucial role of factors such as the connection with the main structure, the mounting position within the main structure, and especially the ratio of the fundamental frequency of the NSCs relative to the main structures in designing for seismic resilience.

CRediT authorship contribution statement

Tran-Van Han: Conceptualization, Data curation, Formal analysis, Methodology, Software, Validation, Writing – original draft, Writing – review & editing. **Sung Chan Kim:** Formal analysis, Writing – re-

view & editing. **Jiuk Shin:** Formal analysis, Writing – review & editing. **Nguyen Huu Cuong:** Formal analysis, Writing – review & editing. **Kihak Lee:** Formal analysis, Funding acquisition, Project administration, Resources, Supervision, Writing – review & editing.

Declaration of competing interest

The authors declare that they have no known competing financial interests or personal relationships that could have appeared to influence the work reported in this paper.

Data availability

The authors do not have permission to share data.

Acknowledgements

This study was completed with financial and technical assistance of Sehong Inc. Ltd located in Republic of Korea. This research was also supported by Basic Science Research Program through the National Research Foundation of Korea (NRF) funded by the Ministry of Education (NRF-2020R1A2C2007195).

References

- [1] R. Villaverde, Seismic design of secondary structures: state of the art, *J. Struct. Eng.* 123 (8) (1997) 1011–1019, [https://doi.org/10.1061/\(ASCE\)0733-9445\(1997\)123:8\(1011\)](https://doi.org/10.1061/(ASCE)0733-9445(1997)123:8(1011)).
- [2] E. FEMA, Reducing the risks of nonstructural earthquake damage, Practical Guide, January 2011.
- [3] C. Adam, P. Fotiu, Dynamic analysis of inelastic primary–secondary systems, *Eng. Struct.* 22 (1) (2000) 58–71, [https://doi.org/10.1016/S0141-0296\(98\)00073-X](https://doi.org/10.1016/S0141-0296(98)00073-X).
- [4] R. Villaverde, Simple method to estimate the seismic nonlinear response of non-structural components in buildings, *Eng. Struct.* 28 (8) (2006) 1209–1221, <https://doi.org/10.1016/j.engstruct.2005.11.016>.
- [5] S.R. Chaudhuri, R. Villaverde, Effect of building nonlinearity on seismic response of nonstructural components: a parametric study, *J. Struct. Eng.* 134 (4) (2008) 661–670, [https://doi.org/10.1061/\(ASCE\)0733-9445\(2008\)134:4\(661\)](https://doi.org/10.1061/(ASCE)0733-9445(2008)134:4(661)).
- [6] I. Tamura, S. Matsuura, R. Shimazu, Yield strength reduction factor of nonlinear sdf systems on the supporting structures, in: *Pressure Vessels and Piping Conference*, vol. 50466, American Society of Mechanical Engineers, 2016, p. V008T08A029.
- [7] V. Vukobratović, P. Fajfar, Code-oriented floor acceleration spectra for building structures, *Bull. Earthq. Eng.* 15 (2017) 3013–3026, <https://doi.org/10.1007/s10518-016-0076-4>.
- [8] J. Obando, D. Lopez-Garcia, Inelastic displacement ratios for nonstructural components subjected to floor accelerations, *J. Earthq. Eng.* 22 (4) (2018) 569–594, <https://doi.org/10.1080/13632469.2016.1244131>.
- [9] H. Anajafi, R.A. Medina, E. Santini-Bell, Inelastic floor spectra for designing anchored acceleration-sensitive nonstructural components, *Bull. Earthq. Eng.* 18 (5) (2020) 2115–2147, <https://doi.org/10.1007/s10518-019-00760-8>.
- [10] A.K. Kazantzi, E. Miranda, D. Vamvatsikos, Strength-reduction factors for the design of light nonstructural elements in buildings, *Earthq. Eng. Struct. Dyn.* 49 (13) (2020) 1329–1343, <https://doi.org/10.1002/eqe.3292>.
- [11] V. Vukobratović, S. Ruggieri, Floor acceleration demands in a twelve-storey rc shear wall building, *Buildings* 11 (2) (2021) 38, <https://doi.org/10.3390/buildings11020038>.
- [12] S. Ruggieri, V. Vukobratović, Acceleration demands in single-storey rc buildings with flexible diaphragms, *Eng. Struct.* 275 (2023) 115276, <https://doi.org/10.1016/j.engstruct.2022.115276>.
- [13] E. Miranda, S. Taghavi, Estimation of seismic demands on acceleration-sensitive nonstructural components in critical facilities, in: *Proceedings of the Seminar on Seismic Design, Performance, and Retrofit of Nonstructural Components in Critical Facilities*, 2003, pp. 29–2.
- [14] C.A. Kircher, It makes dollars and sense to improve nonstructural system performance, in: *Proc ATC 29-2 Seminar on Seismic Design, Performance, and Retrofit of ...*, 2003.
- [15] A. Filiatrault, T. Sullivan, Performance-based seismic design of nonstructural building components: the next frontier of earthquake engineering, *Earthq. Eng. Eng. Vib.* 13 (1) (2014) 17–46, <https://doi.org/10.1007/s11803-014-0238-9>.
- [16] D. Ding, C. Arnold, H. Lagorio, S. Tobriner, S. Rihal, R. Mangum, G. Hezmalhalch, M. Green, A. Watson, D. Mah, et al., Architecture, building contents, and building systems, *Earthq. Spectra* 6 (S1) (1990) 339–377, <https://doi.org/10.1193/1.1585607>.
- [17] L. Qi, M. Kurata, Y. Ikeda, K. Kunitomo, M. Takaoka, Seismic evaluation of two-elevation ceiling system by shake table tests, *Earthq. Eng. Struct. Dyn.* 50 (4) (2021) 1147–1166, <https://doi.org/10.1002/eqe.3390>.
- [18] K.A. Institute, Pohang earthquake damage survey report, 2018.
- [19] G. Magliulo, M. Ercolino, C. Petrone, O. Coppola, G. Manfredi, The Emilia earthquake: seismic performance of precast reinforced concrete buildings, *Earthq. Spectra* 30 (2) (2014) 891–912, <https://doi.org/10.1193/091012EQS285M>.
- [20] E. Miranda, G. Mosqueda, R. Retamales, G. Pekcan, Performance of nonstructural components during the 27 February 2010 Chile earthquake, *Earthq. Spectra* 28 (1_suppl1) (2012) 453–471, <https://doi.org/10.1193/1.4000032>.
- [21] R.P. Dhakal, G.A. MacRae, K. Hogg, Performance of ceilings in the February 2011 Christchurch earthquake, 2011.
- [22] K. Kasai, A. Mita, H. Kitamura, K. Matsuda, T.A. Morgan, A.W. Taylor, Performance of seismic protection technologies during the 2011 Tohoku-oki earthquake, *Earthq. Spectra* 29 (1_suppl) (2013) 265–293, <https://doi.org/10.1193/1.4000131>.
- [23] D. Wang, J. Dai, Z. Qu, X. Ning, Shake table tests of suspended ceilings to simulate the observed damage in the m s 7.0 Lushan earthquake, China, *Earthq. Eng. Eng. Vib.* 15 (2) (2016) 239–249, <https://doi.org/10.1007/s11803-016-0319-z>.
- [24] J. Iyama, S. Matsuo, S. Kishiki, T. Ishida, K. Azuma, M. Kido, T. Iwashita, K. Sawada, S. Yamada, T. Seike, Outline of reconnaissance of damaged steel school buildings due to the 2016 Kumamoto earthquake, *AJ J. Technol. Des.* 24 (56) (2018) 183–188, <https://doi.org/10.3130/ajjt.24.183>.
- [25] D. Perrone, P. Calvi, R. Nascimbene, E. Fischer, G. Magliulo, Seismic performance of non-structural elements during the 2016 central Italy earthquake, *Bull. Earthq. Eng.* 17 (10) (2019) 5655–5677, <https://doi.org/10.1007/s10518-018-0361-5>.
- [26] P. FEMA, 58-2, seismic performance assessment of buildings volume 2: Implementation guide, Federal Emergency Management Agency, Washington, DC, USA, 2012.
- [27] H.H. Hwang, J.-R. Huo, Seismic fragility analysis of electric substation equipment and structures, *Probab. Eng. Mech.* 13 (2) (1998) 107–116, [https://doi.org/10.1016/S0266-8920\(97\)00017-9](https://doi.org/10.1016/S0266-8920(97)00017-9).
- [28] A. Gupta, S. Rustogi, A.K. Gupta, Ritz vector approach for evaluating in-cabinet response spectra, *Nucl. Eng. Des.* 190 (3) (1999) 255–272, [https://doi.org/10.1016/S0029-5493\(99\)00076-X](https://doi.org/10.1016/S0029-5493(99)00076-X), <https://www.sciencedirect.com/science/article/pii/S002954939900076X>.
- [29] S. Rustogi, A. Gupta, Modeling the dynamic behavior of electrical cabinets and control panels: experimental and analytical results, *J. Struct. Eng.* 130 (3) (2004) 511–519, [https://doi.org/10.1061/\(ASCE\)0733-9445\(2004\)130:3\(511\)](https://doi.org/10.1061/(ASCE)0733-9445(2004)130:3(511)).
- [30] K. Porter, G. Johnson, R. Sheppard, R. Bachman, Fragility of mechanical, electrical, and plumbing equipment, *Earthq. Spectra* 26 (2) (2010) 451–472, <https://doi.org/10.1193/1.3363847>.
- [31] S.G. Cho, D. Kim, S. Chaudhary, A simplified model for nonlinear seismic response analysis of equipment cabinets in nuclear power plants, *Nucl. Eng. Des.* 241 (8) (2011) 2750–2757, <https://doi.org/10.1016/j.nucengdes.2011.06.026>, <https://www.sciencedirect.com/science/article/pii/S0029549311005097>.
- [32] S.-J. Wang, Y.-H. Yang, F.-R. Lin, J.-W. Jeng, J.-S. Hwang, Experimental study on seismic performance of mechanical/electrical equipment with vibration isolation systems, *J. Earthq. Eng.* 21 (3) (2017) 439–460, <https://doi.org/10.1080/13632469.2016.1172374>.
- [33] T.-T. Tran, A.-T. Cao, T.-H.-X. Nguyen, D. Kim, Fragility assessment for electric cabinet in nuclear power plant using response surface methodology, *Nucl. Eng. Technol.* 51 (3) (2019) 894–903, <https://doi.org/10.1016/j.net.2018.12.025>, <https://www.sciencedirect.com/science/article/pii/S1738573318306879>.
- [34] H. Son, S. Park, B.-G. Jeon, W.-Y. Jung, J. Choi, B.-S. Ju, Seismic qualification of electrical cabinet using high-fidelity simulation under high frequency earthquakes, *Sustainability* 12 (19) (2020) 8048, <https://doi.org/10.3390/su12198048>.
- [35] N.H. Dinh, S.-J. Lee, J.-Y. Kim, K.-K. Choi, Study on seismic performance of a mold transformer through shaking table tests, *Appl. Sci.* 10 (1) (2020) 361, <https://doi.org/10.3390/app10010361>.
- [36] B.-G. Jeon, H.-Y. Son, S.-H. Eem, I.-K. Choi, B.-S. Ju, Dynamic characteristics of single door electrical cabinet under rocking: source reconciliation of experimental and numerical findings, *Nucl. Eng. Technol.* 53 (7) (2021) 2387–2395, <https://doi.org/10.1016/j.net.2021.01.003>, <https://www.sciencedirect.com/science/article/pii/S1738573321000036>.
- [37] A. Latif, K. Salman, D. Kim, Seismic response of electrical cabinets considering primary-secondary structure interaction with contact nonlinearity of anchors, *J. Nucl. Sci. Technol.* 59 (6) (2022) 757–767, <https://doi.org/10.1080/00223131.2021.2007812>.
- [38] R.J. Merino, D. Perrone, R. Nascimbene, A. Filiatrault, Performance-based seismic classification of acceleration-sensitive non-structural elements, *Earthq. Eng. Struct. Dyn.* 52 (13) (2023) 4222–4244.
- [39] H.V. Tran, S.C. Kim, J. Shin, K. Lee, Experimental study of a novel lighting support system reinforced with a pulley friction damper, *J. Build. Eng.* 52 (2022) 104385, <https://doi.org/10.1016/j.job.2022.104385>.
- [40] H.V. Tran, S.C. Kim, J. Shin, K. Lee, Shaking table testing of an innovative wireway vibration attenuation system, *J. Constr. Steel Res.* 197 (2022) 107477, <https://doi.org/10.1016/j.jcsr.2022.107477>.
- [41] E. ICC, Aci56 acceptance criteria for seismic certification by shake-table testing of nonstructural components, International Code Council Evaluation Service, Country Club Hills, IL, 2010.
- [42] S.-C. Jun, C.-H. Lee, C.-J. Bae, K.-J. Lee, Shake-table seismic performance evaluation of direct-and indirect-hung suspended ceiling systems, *J. Earthq. Eng.* (2020) 1–19, <https://doi.org/10.1080/13632469.2020.1845876>.
- [43] P. Mario, H.K. Young, *Structural Dynamics: Theory and Computation*, 2019.

- [44] F.A. Charney, *Seismic loads: Guide to the seismic load provisions of asce 7-10*, American Society of Civil Engineers, 2015.
- [45] KCSC, *Seismic design code of buildings (kds 41 17 00)*, Ministry of Land, Infrastructure and Transport, Sejong, Korea, 2019.
- [46] U.B. Code, 2000, International Code Council, Inc., Falls Church VA, USA.
- [47] Shake-table testing method for seismic performance evaluation of suspended ceiling, in: Standard, Korea Construction Engineering Development Collaboratory, Management Institute, Gyeonggi-do, ROK, Feb. 2021.
- [48] H.-J. Kim, D.-H. Shin, Shake table test program of cold-formed steel in-plane partition walls, in: *Structures*, vol. 30, Elsevier, 2021, pp. 503–517.
- [49] R.R. Craig Jr, A.J. Kurdila, *Fundamentals of Structural Dynamics*, John Wiley & Sons, 2006.
- [50] ANSYS, *Ansys Theory Reference*, Ansys, Canonsburg, PA, USA, 2021.
- [51] T.-V. Han, Seismic assessment of a novel wireway vibration attenuation system using tri-axial shaking table tests, Phd thesis, Sejong University, Seoul, Republic of Korea, February 2023, available at <https://sejong.dcollection.net/srch/srchDetail/200000658091>.
- [52] ANSYS, *ANSYS mechanical APDL element reference guide*, 2020.
- [53] K.N.R.R. Agency, *Earthquake resistance test method for telecommunication facilities*, Korean National Radio Research Agency, 2015.
- [54] P. Welch, The use of fast Fourier transform for the estimation of power spectra: a method based on time averaging over short, modified periodograms, *IEEE Trans. Audio Electroacoust.* 15 (2) (1967) 70–73, <https://doi.org/10.1109/TAU.1967.1161901>.
- [55] O. Solomon Jr., Psd computations using Welch's method, NASA STI/Recon Technical Report N 92, 1991, p. 23584, <https://www.osti.gov/servlets/purl/5688766>.
- [56] MATLAB, version 9.8.0 (R2020a), The MathWorks Inc., Natick, Massachusetts, 2020.
- [57] G. Housner, P.C. Jennings, Generation of artificial earthquakes, *J. Eng. Mech. Div.* 90 (1) (1964) 113–150, <https://doi.org/10.1061/JMCEA3.0000448>.
- [58] R. Simmons, Calculating grms (root-mean-square acceleration), <https://femci.gsfc.nasa.gov/random/randomgrms.html>, 1997.
- [59] A. Gupta, S.-G. Cho, K.-J. Hong, M. Han, Current state of in-cabinet response spectra for seismic qualification of equipment in nuclear power plants, *Nucl. Eng. Des.* 343 (2019) 269–275, <https://doi.org/10.1016/j.nucengdes.2020.111046>.